BERGISCHE
UNIVERSITÄT
WUPPERTAL

Fachbereich Physik

Maria Gurtner

Cosmic ray anisotropy study with the AMANDA Neutrino Telescope

DISSERTATION
zur Erlangung des Doktorgrades

September 2013

Astroteilchenphysik

Cosmic ray Anisotropy study with the AMANDA Neutrino Telescope

DISSERTATION

zur Erlangung des Doktorgrades

BERGISCHE
UNIVERSITÄT
WUPPERTAL

Fachbereich C – Mathematik und Naturwissenschaften

Unter der Leitung von:
Prof. Dr. Karl-Heinz Kampert

Dem Fachbereich Physik vorgelegt von

Maria Gurtner

im

September 2013

Contents

Chapter 1

Introduction

"Cosmic rays" is the term used to describe any kind of radiation not originating from Earth. This includes particles with extremely high energies which have travelled a long time through the universe. Some may even originate from the big bang bringing lots of information about our universe, which makes them a very interesting object for all kind of studies and therefore, a lot of work has been done in the field of cosmic ray research during the last 100 years: At the beginning of the 20th century, studies on the electric conductivity of gases revealed a residual conductivity. This was first believed to origin from Earth, but in 1910 Father Thomas Wulff took his electroscope on the Eiffel tower and observed a 64% reduction in the leakage rate. This was contradicting the assumption that the atmosphere must have had absorbed the radiation from the ground. Therefore, he concluded, there has to be some kind of radiation coming down through the atmosphere.

With balloon flights up to an altitude of 5700 m, Victor Hess demonstrated the existence of cosmic radiation around 1912. This was the beginning of cosmic ray physics, one discovery followed the other. In 1930, Størmer formulated his theory on the motion of charged particles in the geomagnetic field, two years later, A. H. Compton and independently H. Hoerlin discovered the latitude effect and Carl D. Anderson found a first evidence for the existence of anti-matter (positron). In 1936, Hess and Anderson received the Nobel Prize for their discoveries.

With a cloud chamber in an altitude of 4300m above sea level, Anderson and others discovered the muon in 1936. In 1938 Kohlhörster and Pierre Auger discovered extensive air showers. Fermi postulated his theory on the acceleration of charged particle bouncing off magnetic clouds. In 1965, Penzias and Wilson discovered the 3K background radiation, some months later, Greisen, Kuzmin, and Zatsepin found that if there are cosmic ray protons with an energy above $5 \cdot 10^{19}$ eV (known as the "GZK-cutoff"), they cannot travel long time through the universe before interacting with the cosmic microwave background. In 1991, the Fly's Eye cosmic ray research group observed a cosmic ray event with an energy of $3 \cdot 10^{20}$ eV, in 1994 the AGASA group reported another event with $E = 2 \cdot 10^{20}$ eV.

But even within more than 100 years research on the topic, not all questions have been answered. To one of them, whether cosmic radiation is distributed isotropically or not, this work shall be dedicated. The study of cosmic ray anisotropies can help revealing details about the origin and the propagation of cosmic rays, even about the

composition. Furthermore it can improve the understanding of galactic and intergalactic magnetic fields.

In order to answer the question whether the arrival directions of cosmic rays are distributed isotropically or not, this work will analyse data taken by the **A**ntarctic **M**uon **A**nd **N**eutrino **D**etector **A**rray in the time between 2000 and 2006 in the TeV-energy range. AMANDA is actually not a classical cosmic ray experiment as it is, in first place, a neutrino telescope, consisting of strings with optical modules buried deep under the Antarctic ice. The unique location close to the geographical South Pole brings the advantage of always seeing the same sky. The triggerrate of $\sim 100\,\mathrm{Hz}$ of background muons also allows this study.

Chapter 2

Cosmic rays

The cosmic radiation is now known to consist mainly of protons, but also heavier nuclei, as well as gamma rays and neutrinos.

Most cosmic rays with energies $E < 10^{17}\,\mathrm{eV}$ are believed to origin from inside the galaxy and are therefore known as galactic cosmic rays (GCR). Earth is reached not only by galactic radiation, also high energy particles from the Sun are recorded. These solar cosmic rays (SCR) are accelerated in the solar corona and can reach energies up to 10 GeV in violent explosions on the Sun, like solar flares or coronal mass ejections. Another group of cosmic rays in the low energy region is called "anomalous cosmic rays" (ACR). These are not completely ionised nuclei, drifting as neutral gas into the heliospheric field where they get partly ionised. Above energies around $E = 10^{17}\,\mathrm{eV}$, particles are suspected to origin from outside the Milky Way (EGCR).

This chapter shall invite to a journey with a high energy galactic cosmic ray particle, from its supposed origin through the galaxy into the heliosphere and through the Earth's atmosphere into the detector.

2.1 Origin of cosmic rays

A potential source has to be able to accelerate particles to energies $E > 10^{21}\,\mathrm{eV}$, there should be many of them, they shall be randomly distributed, and they must yield a power-law. Assuming a single source for cosmic rays (which is not a very realistic assumption), the power such a source candidate must provide in order to yield the observed energy spectrum can be estimated using the energy density $\rho \sim 1\frac{\mathrm{eV}}{\mathrm{cm}^3}$, the volume of the galaxy $V = \pi(15\,\mathrm{kpc})^2 \cdot (300\,\mathrm{pc})$, and the mean time the particles stay inside the galaxy $\tau = \tau_{esc} \simeq 6 \cdot 10^6\,\mathrm{y}$ [Hel08]:

$$L = \frac{V\rho}{\tau} \simeq 5 \cdot 10^{40}\,\frac{\mathrm{erg}}{\mathrm{s}} = 5 \cdot 10^{33}\,\mathrm{W}, \tag{2.1}$$

The luminosity of the Sun is, in comparison, $4 \cdot 10^{26}\,\mathrm{W}$.

2.1.1 Cosmic ray source candidates

Up to $E \sim 10^{17}\,\mathrm{eV}$, it is widely accepted for the bulk of cosmic rays to origin from galactic sources.

- Supernovae:
  - Energy per explosion $\sim 10^{44}$ J.
  - Duration: few hours up to days.
  - Power: $\sim 10^{38} - 10^{40}$ W

  The mean rate of supernova explosions in the Milky Way is $\sim 1/30$ y, with a mean power of 10^{35} W, so only 1% of efficiency is sufficient to maintain a constant cosmic ray energy density of 1ev/cm^3.

- Young pulsars (rotating neutron stars as SN-remnants), initial rotational energy typically $\sim 10^{46}$ J.

- Double star systems: Accretion on a neutron star or black hole.

Above $E \sim 10^{17}$ eV, cosmic rays are believed to origin from outside the galaxy. Extragalactic source candidates are e. g. active galactic nuclei: Most prominent galaxies with active nuclei are e.g. the Seyfert galaxies, quasars, BL-Lac, and others. AGNs could possibly be able to accelerate charged particles to energies beyond 10^{20} eV [Hel08].

All of these are source candidates, the question about the origin of the highest energy cosmic rays is not finally answered up to today.

2.1.2 Acceleration

The most popular acceleration mechanism was proposed by Enrico Fermi in 1949 ([Fer49]) and describes the acceleration of charged particles as a stochastic process when particles undergo a certain kind of "scattering" within magnetised clouds. Based on Fermis assumptions, e.g. [ALS77], [Bel78a] and [Bel78b],[Kry77] postulated an acceleration process in strong shock waves, nowadays referred to as "First order Fermi acceleration", while the stochastic process described by Fermi is known as "Second order Fermi acceleration".

Fermi acceleration

Fermi acceleration describes the energy gain ΔE of a particle with velocity v inside some kind of "accelerator" which is moving with velocity u. Considered is a process in which a particle increases its energy about $\Delta E = \beta E$ at any encounter with the "accelerator" and with P as the probability that the particles remains within the acceleration region after the encounter. Consequently, after n encounters there will be (adopted from [Lon81a])

$$N = N_0 P^k \tag{2.2}$$

particles with energies

$$E = E_0 \beta^k. \tag{2.3}$$

Eliminating n from the equations above brings

$$\frac{\ln(N/N_0)}{\ln(E/E_0)} = \frac{\ln P}{\ln \beta}$$

which leads to

$$\frac{N}{N_0} = \left(\frac{E}{E_0}\right)^{\ln P/\ln \beta} \tag{2.4}$$

and yields a power law in the energy spectrum of the form:

$$N(E)\mathrm{d}E = \text{const} \cdot E^{-x}\mathrm{d}E \tag{2.5}$$

In all above equations, $\beta = 1 + (\alpha/M)$, with α/M being the energy gain per encounter, and P is related to the escape time τ_{esc}.

In his original paper, Fermi describes the "accelerator" as randomly distributed, magnetised clouds with mass M moving isotropically with velocity V where the particle with mass m with velocity v enters the cloud and undergoes a kind of "collisionless scattering" on the irregularities of the magnetic field.

For the following calculations it is assumed that the mass M of the cloud is infinite so that its velocity V is not changed by the encounter with the particle whose velocity is assumed to be $v \approx c$. Within the centre of momentum frame moving with velocity V, the energy of the particle before the collision is

$$E' = \gamma v(E + Vp\cos\theta) \text{ with } \gamma v = \left(1 - \frac{V^2}{c^2}\right)^{-1/2}. \tag{2.6}$$

In the collision, the energy E' is preserved, the momentum in x-direction is reversed. This leads, when transforming back to observers frame, to

$$E'' = \gamma v(E' + Vp'). \tag{2.7}$$

With the x component of the relativistic three-momentum in the centre of momentum frame

$$p'_x = p'\cos\theta' = \gamma v\left(p\cos\theta + \frac{VE}{c^2}\right)$$

and $p_x/E = v\cos\theta/c^2$, Eq. (2.7) is

$$E'' = \gamma^2 vE\left[1 + \frac{2Vv\cos\theta}{c^2} + \left(\frac{V}{c}\right)^2\right].$$

Expanded to second order this leads to the change of energy of the particle:

$$E'' - E = \Delta E = \frac{2Vv\cos\theta}{c^2} + 2\left(\frac{V}{c}\right)^2 \tag{2.8}$$

By averaging over θ in the relativistic limit gives the average energy gain per collision:

$$\left\langle \frac{\Delta E}{E} \right\rangle = \frac{8}{3} \left(\frac{V}{c} \right)^2 . \tag{2.9}$$

This result is usually referred to as "Second order Fermi acceleration". In order to arrive at the expected power law, some assumptions need to be taken. First it is assumed that the mean free path between clouds along a field line is L. Then the time between collisions is $L/(c \cos \phi)$ with ϕ the pitch angle of the particle with respect to the magnetic field direction. Averaging over ϕ results in the average time between collisions which is $2L/c$. A typical energy increase is then

$$\alpha E = \frac{\mathrm{d}E}{\mathrm{d}t} = \frac{4}{3} \left(\frac{V^2}{cL} \right) E. \tag{2.10}$$

Assuming further that there is a characteristic time for a particle to stay inside the acceleration region τ_{esc} and using the diffusion-loss equation [Lon81a]:

$$\frac{\mathrm{d}N(E)}{\mathrm{d}t} = \frac{\mathrm{d}}{\mathrm{d}E} \left[b(E) N(E) \right] + Q(E,t) + D \nabla^2 N(E) \tag{2.11}$$

Looking for the steady-state solution ($\frac{\mathrm{d}N(E)}{\mathrm{d}t} = 0$), neglecting diffusion ($D \nabla^2 N(E) = 0$) and sources ($Q(E,t) = 0$) using the solution from Eq. (2.11) for $N(E)$ in equilibrium and inserting the energy loss term from Eq. (2.10) for $b(E)$ Eq. (2.11) simplifies to

$$-\frac{\mathrm{d}}{\mathrm{d}E} [\alpha E N(E)] - \frac{N(E)}{\tau_{esc}} = 0$$

which gives by differentiating:

$$\frac{\mathrm{d}N(E)}{\mathrm{d}E} = -\left(1 + \frac{1}{\alpha \tau_{esc}} \right) \frac{N(E)}{E}$$

and this leads to a power law as described in Eq. (2.5) where $x = 1 + (\alpha \tau_{esc})^{-1}$.

Another physical situation describes the "First order Fermi acceleration"(adopted from [Lon81a], see also references therein). Here a plane shock front moves with velocity U and the gas behind the shock moves with velocity $\frac{3}{4}U$ relative to the upstream gas.

The average increase of energy of a particle crossing the shock from the upstream to the downstream side. The gas at the downstream side approaches with velocity $V = \frac{3}{4}U$ and the energy of the particle when passing into the downstream region is

$$E' = \gamma v (E + p_x V) \tag{2.12}$$

The x component of the momentum shall be perpendicular to the shock. When the shock is non-relativistic ($V \ll c$, $\gamma v = 1$), but the particle is relativistic, the change of energy of the particle is

$$\frac{\Delta E}{E} = \frac{V}{c} \cos \theta$$

The probability that the particles which cross the shock arrive at angle θ per unit time is given by the number of particles within the angles θ and $\theta + \mathrm{d}\theta$, which is proportional to $\sin\theta \mathrm{d}\theta$. The rate at which they approach the shock front, which is proportional to the x-component of their velocities, is $c\cos\theta \mathrm{d}\theta$. This leads to the average energy gain when crossing the shock from up- to downstream

$$\left\langle \frac{\Delta E}{E} \right\rangle = \frac{V}{c} \int_0^{\pi/2} 2\cos^2\theta \sin\theta \mathrm{d}\theta = \frac{2}{3}\frac{V}{c} \tag{2.13}$$

where the particles velocity vector is randomised and it repasses the shock, gaining another increase of energy of $\frac{2}{3}(V/c)$, so that one round-trip the energy increases on average by

$$\left\langle \frac{\Delta E}{E} \right\rangle = \frac{4}{3}\frac{V}{c} = \frac{U}{c} \tag{2.14}$$

In order to arrive at the power law from this point, β and P from Eq.(2.4) can be evaluated. As β denotes the increase of energy of the particle, it can be calculated directly from Eq.(2.14) as

$$\beta = \frac{E}{E_0} = 1 + \frac{4V}{3c} \tag{2.15}$$

The value for P can be evaluated using classical kinetic theory from which it follows that the number of particles crossing the shock is $\frac{1}{4}Nc$. Downstream of the shock, particles are swept away from the shock at a rate $NV = \frac{1}{4}NU$ and the fraction of particles lost per unit time is

$$\frac{1/4NU}{1/4Nc} = \frac{U}{c}$$

then $P = 1 - (U/c)$. Now, using Eq.(2.5) with $x = 1 + (\ln P/\ln\beta)$ and the results obtained for β and P, this process actually describes a differential energy spectrum as:

$$N(E)\mathrm{d}E \propto E^{-2}\mathrm{d}E \tag{2.16}$$

In both scenarios, the maximum energy a particle can achieve is limited by the finite lifetime of the accelerator. For acceleration processes at the shock wave of a supernova explosion, very rough estimations lead to a maximum energy of $\propto 100\,\mathrm{TeV}$ [Gai90]. This number can be raised by one or two order of magnitudes depending on the constellation of the environment of the shock or magnetic field configurations. Candidates for the acceleration up to $\propto 10^{20}\,\mathrm{eV}$ are assumed to be located outside the galaxy. Those might be gamma ray bursts or active galactic nuclei.

2.2 CR Propagation in the interstellar medium

2.2.1 The interstellar medium

"Interstellar medium (ISM)" is the term for anything in between the stars. Knowledge of the ISM is of great importance to study a lot of phenomenons in the galaxy, as its

magnetic fields influences charged particles. It can be divided into the interstellar gas and the interstellar magnetic fields. The ISM is far from equilibrium, moreover, there are a lot of different states, densities, temperatures, etc. Tab. 2.1 shows a compilation of the most prominent phases of the interstellar gas. The interstellar magnetic field has a regular and a turbulent component. The regular magnetic field follows the spiral pattern of the galaxy and its strength is $\sim 1-3\mu$G. If a charged particle enters the influence of a magnetic field it is deflected by it and eventually bound on a circle of the particles gyro- or Larmorradius given by the charge and the energy of the particle, and the strength of the magnetic field. If the particle is of ultra high energy ($> 10^{18}$ eV), the gyroradius is larger than the thickness of the galactic disk and the particle escapes. Particles with $E < 10^{18}$ eV are bound on circles by the galactic magnetic field and stay for a long time inside the galaxy.

A simplified, but still complicated description of charged particle propagation in the ISM is given by the transfer equation (Eq. (2.17)-Eq. (2.23)). The Transfer equation for cosmic rays of a particular species i, is a compilation of sources and sinks of cosmic rays in the galaxy and describes the propagation of cosmic rays (adapted from [Gai90]):

$$\frac{\partial N}{\partial t} = \underbrace{\nabla \cdot (D_i \nabla N_i)}_{\text{diffusion}} \tag{2.17}$$

$$- \underbrace{\frac{\partial}{\partial E_i}\left[N_i \frac{\mathrm{d}E_i}{\mathrm{d}t}\right]}_{\text{energy gain/loss}} \tag{2.18}$$

$$- \underbrace{\nabla \cdot u N_i(E)}_{\text{convection}} \tag{2.19}$$

$$+ \underbrace{Q_i(E,t)}_{\text{source term}} \tag{2.20}$$

$$- \underbrace{\left(\frac{v\rho\sigma_i}{m} + \frac{1}{\gamma\tau_i}\right) N_i}_{\text{interaction losses}} \tag{2.21}$$

$$+ \underbrace{\frac{v\rho}{m} \sum_{k \geq i} \int \frac{\mathrm{d}\sigma_{i\to k}(E,E')}{\mathrm{d}E} N_k(E') \mathrm{d}E'}_{\text{spallation}} \tag{2.22}$$

$$+ \underbrace{\sum_{k \geq i} \frac{N_k}{\gamma \tau_{ik}}}_{\text{decay of nuc.parents}} \tag{2.23}$$

The first term (Eq. (2.17)), describes the diffusion. Cosmic rays of energies $\sim 10^9 - 10^{14}$ eV, are most probably accelerated in shocks from supernova remnants. According to first law of Fick, the particle density of the flux ($J\left(\frac{\mathrm{mol}}{\mathrm{m^2 s^2}}\right)$) has to be proportional to the gradient of the concentration ($\nabla N[\mathrm{mol} \cdot \mathrm{m}^{-4}]$):

$$J = -D \cdot \nabla N. \tag{2.24}$$

Name	Main constituent	Detected by	Fraction by volume	Fraction by mass	Part. density $[\mathrm{m}^{-3}]$	Temp. [K]
Molecular clouds	H_2, CO, CS, etc.	Molecular lines, dust emission	$\sim 0.5\%$	40%	$\geq 10^9$	10-30
Diffuse clouds, HI clouds, cold neutral medium	H,C, O with some ions, C^+, Ca+	21-cm emission & absorption	5%	40%	$10^6 - 10^8$	80
Intercloud medium	H, H^+, e^-, (ionisation fraction 10-20%)	21-cm emission & absorption, Hα emission	40%	20%	$10^5 - 10^6$	8000
Coronal gas	H^+, e^-, highly ionised species, O^{5+}, C^{3+}, etc.	OVI, soft X-rays $0.1 - 2\,\mathrm{keV}$	$\sim 50\%$	0.1%	$\sim 10^3$	$\sim 10^6$

Table 2.1: The principal phases of the interstellar gas [Lon81a]

With the diffusion coefficient $D = \frac{1}{3} \cdot \lambda_0 \cdot v$, where λ_0 is mean free path for diffusion, and v the velocity of the particle, the diffusion equation can be written in the form

$$\frac{N}{t} = \nabla \cdot (D \cdot \nabla N). \tag{2.25}$$

Eq. (2.18) takes into account the energy gains and losses upon the energy spectrum of the particles, while Eq. (2.19) describes the convection with velocity u. Q_i (Eq. (2.20)) is the rate of injection of particle species i from sources per unit volume. Eq. (2.21) accounts for losses due to interactions with the interstellar medium and decay. The last two terms describe spallation (Eq. (2.22)) and decay of nuclear parents (Eq. (2.23)), respectively.

2.2.2 Propagation models

This is only a small compilation of the most famous propagation models. For references and an overview over other models see [Ces80].

Leaky-Box-Model

The Milky Way is a spiral galaxy with a radius of $\sim 15\,\mathrm{kpc}$ and a mean gas density of 1 proton per $\mathrm{cm}^3 = 1.7 \cdot 10^{-24}\,\mathrm{g/cm}^3$. The magnetic field strength is around $3 \cdot 10^{-10}\,\mathrm{T}$. As the galaxy is a very complicated structure, the transfer equation (Eq. (2.17)-Eq. (2.23)) can hardly be solved. The "Leaky-Box-Model" tends to simplify the equation with some assumptions:

1. Cosmic rays propagate freely inside the confinement volume during a mean time (τ_{esc}) until they escape. This simplifies the diffusion term (Eq. (2.17)) to $\frac{N_i(E)}{\tau_{esc}}$.
2. Cosmic rays are in an equilibrium inside the galaxy, a mean number of sources are distributed homogeneously, so $\frac{\partial N}{\partial t} = 0$.
3. Energy gains and losses (Eq. (2.18)) are neglected.
4. Approximation for the spallation process: Energy per nucleon of the fragments does not change.

With $\lambda_{esc} = \rho\beta c\tau_{esc}$, $\lambda_{int} = \left(\frac{v\rho\nabla_i}{m} + \frac{1}{\gamma\tau_i}\right)^{-1}$, and $\lambda_{i,k} = \frac{m}{v\rho\sigma_{i,k}}$, the transfer equation is replaced by the leaky-box-model-equation:

$$\underbrace{N_i \left[\frac{1}{\lambda_{esc}(E)} + \frac{1}{\lambda_{int}(E)}\right]}_{\text{gains}} = \underbrace{Q_i(E_i) + \sum_{k>i} \frac{N_k(E)}{\lambda_{i,k}}}_{\text{losses}} \tag{2.26}$$

In Eq. (2.26), λ_{int} and $\lambda_{i,k}$ are known from accelerator experiments on Earth. Assuming all nucleons have similar propagation history,

$$\lambda_{esc} \simeq 11\,\mathrm{g/cm}^2 \cdot \beta \left(\frac{4\,\mathrm{GV}}{R}\right)^{\delta}$$

for $R > 4\,\mathrm{GV}$ and $\delta \simeq 0.6$, where $R = \frac{pc}{Ze}$, the magnetic rigidity. For nuclei mainly not produced by spallation (e.g. protons, iron), $\sigma_{i,k} \simeq 0$, Eq. (2.26) becomes solvable:

$$N_p(E) = Q_p(E) \cdot \frac{\lambda_{esc}}{1 + \lambda_{esc}/\lambda_{int}} \tag{2.27}$$

For protons, $\lambda_{int}^{p} \simeq 90 \frac{\mathrm{g}}{\mathrm{cm}^2} >> \lambda_{esc}$, therefore, $N_p(E) \propto Q_p(E) \cdot E^{-\delta}$. For iron, $\lambda_{int}^{Fe} \simeq 2 \frac{\mathrm{g}}{\mathrm{cm}^2} << \lambda_{esc}$ (for small energies), which leads to $N_{Fe}(E) \propto Q_{Fe}$.

Nested leaky-box-model

In the nested leaky-box-model [CW73] it is assumed, that there are small confinement regions of relatively high density close to the sources, where particle diffuse for a short, but energy-dependent time. The energy dependence is attributed to energy dependent leakage from the source region, given by $\lambda_1(E)$. The galaxy is considered to be an outer volume in which the nuclei traverse another amount of matter, λ_2. Most values can be explained in the nested leaky-box-model as well as in the leaky-box-model, if the outer volume is chosen large enough. An observer inside a source region would measure a differential spectrum of $\propto E^{-(\alpha+\delta)}$ due to energy dependent leakage out of the source. But as the Earth is not considered to be inside a source region, the measured spectrum fits to predictions.

Closed galaxy model

The closed galaxy model [RP75]is a variation of the nested leaky-box-model in which the Earth is indeed inside the source region, as the inner volume is considered to be the local spiral arm of the galaxy. The large outer volume is completely closed.

Diffusion models

As the name suggests these are models where the diffusion equation (Eq. (2.17)-Eq. (2.23)) is solved without treating the diffusion operator as a constant. These models are physically more realistic than the various leaky-box-models, but for many purposes, they are equivalent. The main difference between the models is, that in the diffusion models, other than in a leaky-box-model, there is a diffusion and where there is diffusion, there are density gradients and there is also anisotropy. In the leaky-box-model, the distribution of cosmic rays is uniform inside the confinement volume in steady state.

2.3 Cosmic rays at the top of the atmosphere

2.3.1 Composition

Considering particle types, $\sim$ 98% of the cosmic radiation consist of nuclei (mostly protons). The other $\sim$ 2% are filled by electrons, photons, neutrinos and others.

The $\sim 98\%$ are mainly made of protons, but heavier nuclei also share the part. Comparing their abundances with the elemental abundance in the solar system, as it is shown in Fig. 2.1, reveals two striking differences. The first one is the abundance of heavier nuclei ($Z > 1$), compared to the one of protons which is significantly higher in cosmic rays than in the solar system. This feature is not completely understood, a possible reason could be that hydrogen is quite hard to ionise, but it could also be an indicator for a different composition of the sources of cosmic rays.

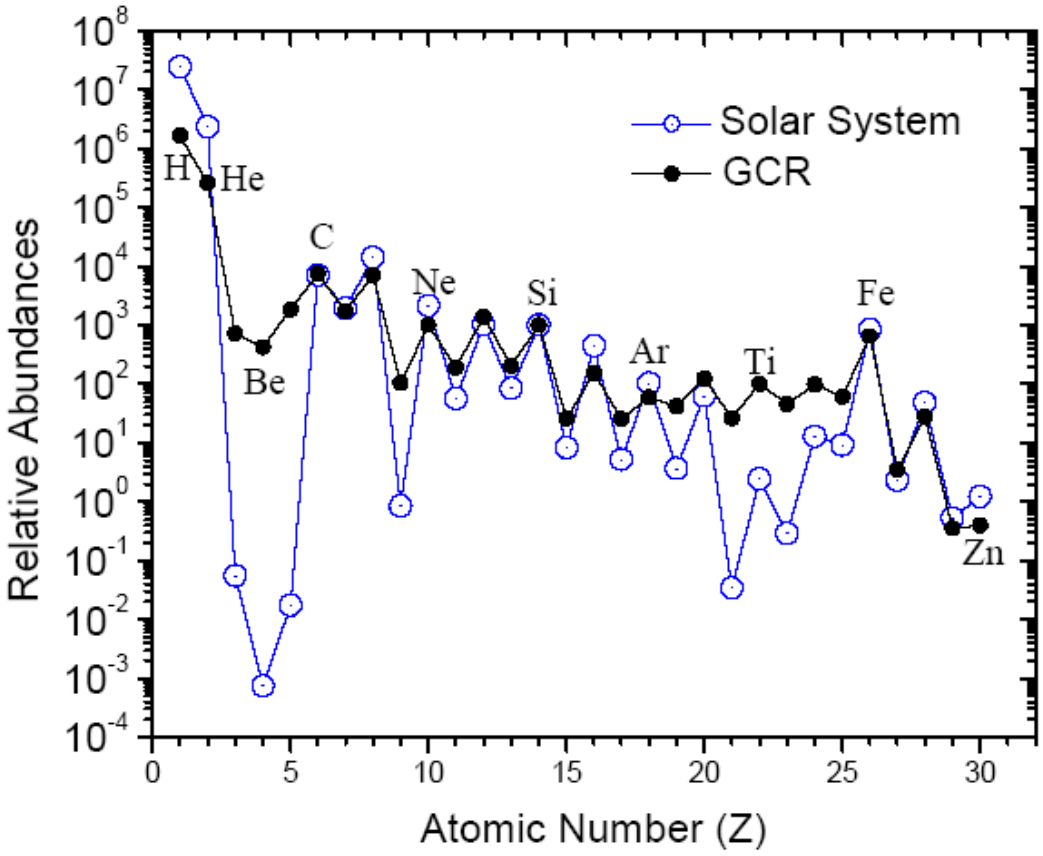

Figure 2.1: Cosmic abundances of elements compared with solar system abundances at the top of the atmosphere rel silicon [Sim83]

The second difference is in the relative abundances of the two groups of elements Li, Be, B, and Sc, Ti, V, Cr, Mn. These elements are hardly present in the solar system, but they are very abundant in the cosmic radiation, as they are spallation products of carbon and oxygen (Li, Be, B), and iron (Sc, Ti, V, Cr, Mn) [Gai90]. This effect is well-known and gives information about propagation and residence times of cosmic rays inside the galaxy.

2.3.2 Energy

The energy of cosmic rays spreads over more than 10 decades. Fig. 2.2 shows the differential all-particle energy spectrum of the cosmic radiation at the top of the atmosphere.

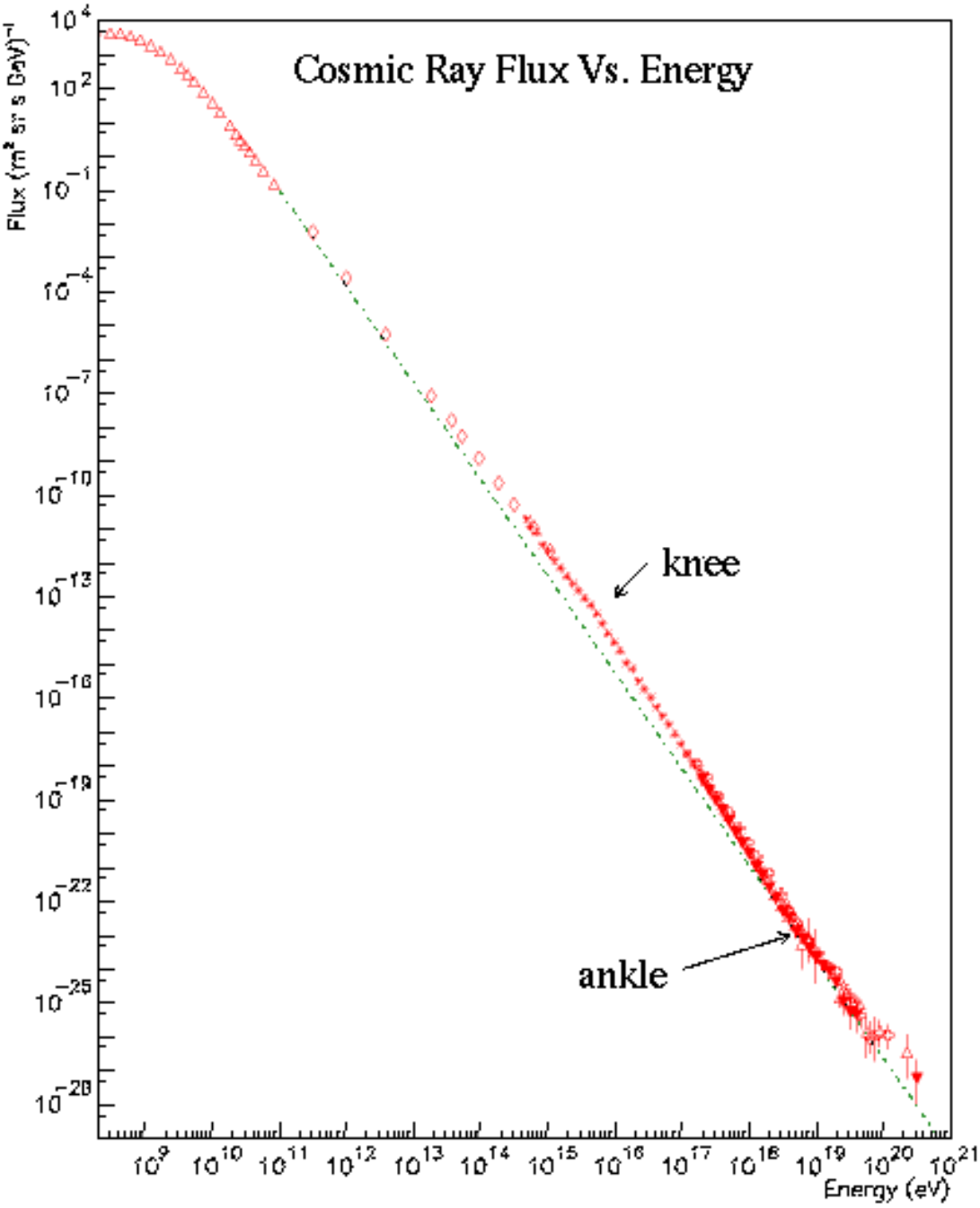

Figure 2.2: All-particle energy spectrum for cosmic rays [Swo97]

The differential flux is described by the number of particles per unit time, energy,

area, and solid angle (Fig. 2.2).

$$I(E) = \frac{\mathrm{d}^4 N}{\mathrm{d}t\,\mathrm{d}E\,\mathrm{d}A\,\mathrm{d}\Omega} \tag{2.28}$$

The cosmic ray energy spectrum parametrises like:

$$I(E) \sim E^{-\gamma}\,\frac{\text{nuclei}}{\text{cm}^2\ \text{s sr GeV}} \tag{2.29}$$

In Eq. (2.29), E is the energy, and γ the spectral index. Below $E \approx 10\,\text{GeV}$, the flux undergoes the solar modulation as seen in Fig. 2.2. This part of the spectrum depends on solar activity. During phases with high solar activity, the flux of galactic cosmic rays with energies below 10 GeV is suppressed by the heliosphere. Above 10 GeV the particles enter the heliosphere independently from solar activity [Gai90]. The spectral index for energies > 10 GeV is not constant over the whole range:

$$\begin{aligned}
10^{10}\ \text{eV} \leq\ & E\ \leq 3\cdot 10^{15}\ \text{eV} \rightarrow \gamma = 2.7\\
3\cdot 10^{15}\ \text{eV} \leq\ & E\ \leq 3\cdot 10^{18}\ \text{eV} \rightarrow \gamma = 3.0\\
3\cdot 10^{18}\ \text{eV} \leq\ & E\ \leq 5\cdot 10^{19}\ \text{eV} \rightarrow \gamma = 2.7\\
& E\ > 5\cdot 10^{19}\ \text{eV} \rightarrow \gamma \sim 4.5\ ([\text{Pie08}])
\end{aligned}$$

The all-particle spectrum follows a power law in the order of $\frac{\mathrm{d}N}{\mathrm{d}E} = E^{-\gamma}$ with $\gamma \sim 2.7$ up to $E \sim 10^{15}$ eV. Above this energy, the spectrum steepens to $\gamma \sim 3$, this change in the slope is usually referred to as the knee of the spectrum. At very high energy, $E \sim 10^{18}$ eV, the spectrum flattens again to a spectral index of $\gamma \sim 2.7$. This region is called the ankle.

An estimation of the energy density can be obtained by integrating the differential flux Eq. (2.28), according to [Gai90]:

$$\text{Flux}\left[\frac{\text{particles}}{\text{cm}^2\,\text{s}\,\text{sr}}\right] = \frac{\rho_{cr}\beta c}{4\pi} \tag{2.30}$$

where ρ_{cr} denotes the number density of cosmic rays, which gives, when integrated over the energy, the energy density.

$$\rho_E = \int E\mathrm{d}E\rho_{cr}(E) = 4\pi \int E\frac{\mathrm{d}N}{\mathrm{d}E}\frac{\mathrm{d}E}{\beta\,c} = \int \frac{4\pi E^2}{\beta\,c}\frac{\mathrm{d}N}{\mathrm{d}E}\mathrm{d}(\ln E). \tag{2.31}$$

So far, the energy density is derived from the cosmic ray flux at the top of Earth's atmosphere, which is different from the flux of galactic cosmic rays, due to the position of the Earth inside the heliosphere. The energy density in the interstellar medium can be inferred from observations at different solar activity phases with large uncertainties, as a rough estimation could be a factor of two between the energy density in the galaxy and the one measured from cosmic rays at Earth.

2.4 Cosmic ray interactions in the atmosphere

Compared to space, the Earth's atmosphere is a very dense medium consisting mainly of nitrogen and oxygen molecules. When entering this medium, cosmic ray particles will undergo interactions with the atoms and electrons of these molecules. In every interaction, new particles are generated which interact further leading to cascades of interaction, called cosmic ray air showers. Depending on energy, charge, and mass, different interaction channels are possible.

2.4.1 Ionisation losses

Due to the electromagnetic forces between the incoming particle and the electrons within the atomic shells of the atoms of the atmosphere, latter can be torn off their atoms. In this process, some energy is passed from the high energy particle to the stationary electron in the atomic shell.

The Bethe-Bloch-Equation describes the energy loss of a high energy particle passing through matter, due to excitation and ionisation of atoms in the surrounding matter. Eq. (2.32) shows the Bethe-Bloch-Equation for a massive, high energy particle of velocity v and charge z passing through a dense material with electron density N_e and ionisation potential I [Lon81b].

$$-\frac{\mathrm{d}E}{\mathrm{d}x} = \frac{z^2 e^4 N_\mathrm{e}}{4\pi\varepsilon_0^2 m_\mathrm{e} v^2}\left[\ln\left(\frac{2\gamma^2 m_\mathrm{e} v^2}{\overline{I}}\right) - \frac{v^2}{c^2}\right], \tag{2.32}$$

where N_e is the electron density, and $\overline{I}$ is the ionisation potential, the factor has to be treated as a parameter to be fitted to laboratory experimental data.

Eq. (2.32) depends only on the velocity and charge of the incoming particle but it is only valid under the assumption that the incident particle is much heavier than an electron.

2.4.2 Radiation losses

Bremsstrahlung

Bremsstrahlung is the radiation of an accelerated electron within the electrostatic field of ions or nuclei. In this case, the ion or nucleon is in rest, while the electron moves within the field. The intensity spectrum of relativistic bremsstrahlung with some approximations derived by [Lon81b] is:

$$I(\omega) = \frac{Z^2 e^6 N}{12\pi^3\varepsilon_0^3 c^3 m_e^2 v}\ln\left(\frac{192v}{Z^{1/3}c}\right) \tag{2.33}$$

The energy loss suffered from a relativistic electron in the electrostatic field of a nucleus can be obtained by integrating the intensity spectrum Eq. (2.33) over the frequency ω and by considering $v = c$:

$$-\left(\frac{\mathrm{d}E}{\mathrm{d}t}\right) = \frac{Z^2 e^6 N E}{12\pi^3 \varepsilon_0^3 c^3 m_e^2 c^4 \hbar} \ln\left(\frac{192}{Z^{1/3}}\right) \tag{2.34}$$

Eq. (2.34) is derived using several approximations, e. g. were electron-electron interactions between the relativistic electron and the ones bound to the nucleus neglected. The proper formula comes from Bethe and Heitler:

$$-\left(\frac{\mathrm{d}E}{\mathrm{d}t}\right) = \frac{Z(Z+1.3) e^6 N E}{16\pi^3 \varepsilon_0^3 c^3 m_e^2 c^4 \hbar} \left[\ln\left(\frac{183}{Z^{1/3}}\right) + \frac{1}{8}\right] \tag{2.35}$$

The relativistic bremsstrahlung losses are of exponential form ($-\mathrm{d}E/\mathrm{d}x \propto E$), and it is therefore possible to define a radiation length X_{brems} over which the electron loses $(1 - 1/e)$ of its energy: $-\frac{\mathrm{d}E}{\mathrm{d}x} = \frac{E}{X_{\mathrm{brems}}}$.

For interactions in the Earth's atmosphere, it is convenient to describe the interaction length in terms of kilograms per square meter, $\xi_0 = \rho X_{\mathrm{brems}}$ through which the electron passes.

$$-\frac{\mathrm{d}E}{\mathrm{d}\xi} = -\frac{\mathrm{d}E}{\mathrm{d}t}\frac{1}{\rho c} = \frac{E}{\rho X_{\mathrm{brems}}} = \frac{E}{\xi_0} \tag{2.36}$$

The first term in Eq. (2.36), $-\mathrm{d}E/\mathrm{d}\xi$, describes the total energy loss or "stopping power". At lower energies when the electron becomes non-relativistic, they lose their energy mainly by ionisation, as the energy increases and the particle become relativistic, bremsstrahlung losses become dominant. It is possible to define a "critical energy", E_{c}, where the principal loss mechanism changes from ionisation losses to bremsstrahlung losses.

Cherenkov radiation

If a charged particle passes through a medium, it polarities the atoms of the medium along the path. If the particles speed exceeds $c = \frac{c_0}{n}$, the speed of light in that medium (c_0 the speed of light in vacuum and n the refraction index) i.e. $\beta \geq 1/n$, the polarization is effected asymmetrically and radiation is emitted. The angle θ under which the radiation is emitted depends on the velocity of the particle and the refraction index of the medium [Lon81b]:

$$\cos\theta = \frac{1}{n\beta} \tag{2.37}$$

Fig. 2.3 shows the development of a conical wavefront as a superposition of spherical waves along the particles trajectory. The radiation is emitted perpendicular to the wave front.

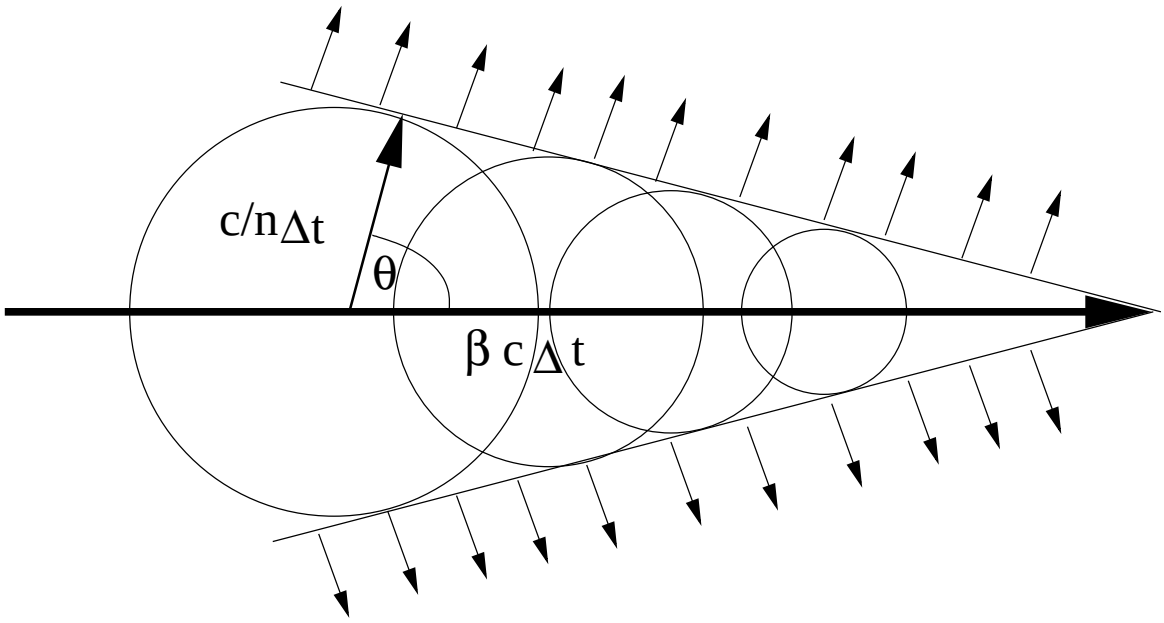

Figure 2.3: Formation of Cherenkov wave front along a particles trajectory

The threshold energy for this process is

$$E_{th} = \frac{m_0 c^2}{\sqrt{1 - \frac{1}{n^2}}} \tag{2.38}$$

and the number of photons emitted along the path

$$\frac{\mathrm{d}^2 N}{\mathrm{d}x \mathrm{d}\lambda} = \frac{2\pi\alpha z^2}{\lambda^2} \sin^2 \theta. \tag{2.39}$$

2.4.3 Interactions of high energy photons

Photoelectric absorption

For photons with energies well below the kinetic energy of the electrons in the surrounding matter, this is the principal loss process.

The atomic shells have discrete energy levels where $\hbar\omega = E_\mathrm{I}$, where $\hbar\omega$ is the energy of the incident photon and E_I the binding energy of the electron. If Photons with energy $\hbar\omega \geq E_\mathrm{I}$ interacts with surrounding atoms, electrons are ejected from their atomic shell. The residual energy $(\hbar\omega - E_\mathrm{I})$ is then passed to the electron as kinetic energy $(m_\mathrm{e} v^2)$ [Lon81b].

Scattering processes

The main scattering processes important at cosmic ray energies are the Compton scattering and inverse Compton scattering.

- **Compton scattering:**
  When high energy photons (e.g. X-rays) scatter on stationary electrons inside the atomic shells of the atoms in the medium surrounding, they pass some of their energy to the electron and their wavelengths increases. The increase in the wavelength of the photon is

$$\frac{\Delta\lambda}{\lambda} = \frac{\hbar\omega}{m_\mathrm{e}c^2}(1-\cos\alpha) \tag{2.40}$$

  If the photons energy exceeds the kinetic energy of the electron ($\hbar\omega \geq m_\mathrm{e}c^2$), the cross-section of the scattering is given by Klein-Nishima:

$$\sigma_{\mathrm{K-N}} = \pi r_\mathrm{e}^2 \frac{1}{\varepsilon}\left\{\left[1-\frac{2(\varepsilon+1)}{\varepsilon^2}\right]\ln(2\varepsilon+1)+\frac{1}{2}+\frac{4}{\varepsilon}-\frac{1}{2(2\varepsilon+1)}\right\} \tag{2.41}$$

- **Inverse Compton scattering:**
  Inverse Compton scattering is when low energy photons scatter on relativistic electrons. In this process, the electrons lose energy rather than gain while the photons do gain. Therefore, it is called "inverse Compton scattering". When low energy photons scatter on relativistic electrons, it is evident that there is a maximum energy that the photon can gain in a fully elastic head-on collision:

$$(\hbar\omega)_{\max} = \hbar\omega\gamma^2\left(1+\frac{v}{c}\right)^2 \approx 4\gamma^2\hbar\omega_0$$

  The average energy of the scattered photons is

$$\hbar\omega = \frac{4}{3}\gamma^2\left(\frac{v}{c}\right)^2\hbar\omega_0 \approx \frac{4}{3}\gamma^2\hbar\omega_0 \tag{2.42}$$

  The photon gains γ^2 energy in average. This makes this process very important for astroparticle physics as photons can be accelerated to very high energies.

$\mathrm{e}^+ - \mathrm{e}^-$-pair production

In the presence of a nucleus, photons with very high energy, $E_\mathrm{Ph} > 2m_\mathrm{e}c^2$, can produce an $\mathrm{e}^+\,\mathrm{e}^-$-pair. This process cannot take place in the vacuum, as energy and momentum cannot be conserved simultaneously.

It needs a third party, e.g. a nucleus from the surrounding medium where to transfer some of the energy or momentum to.

Cross-section of $\mathrm{e}^+ - \mathrm{e}^-$-pair production is [Lon81b]:

$$\sigma_\mathrm{pair} = \alpha r_\mathrm{e}^2 Z^2\left[\frac{28}{9}\ln\left(\frac{183}{Z}\right)-\frac{218}{27}\right]\ \mathrm{m^2 atom^{-1}}. \tag{2.43}$$

Similar to bremsstrahlung, a radiation length can be formulated:

$$X_\mathrm{pair} = \frac{\rho}{N_\mathrm{i}}\sigma_\mathrm{pair} = \frac{M_\mathrm{A}}{N_0\sigma_\mathrm{pair}} \tag{2.44}$$

where $N_\mathrm{i}i$ is the number density of nuclei, M_A the atomic mass, and N_0 the Avogadro number.

2.4.4 Neutrino interactions

Neutrinos are chargeless leptons. They interact with matter via charged current reactions. The charged current reaction is a weak interaction where leptons interact with quarks exchanging a charged W-boson. Within this interaction, a charged lepton and a hadronic cascade is produced.

$$\nu + \text{nucleus} \rightarrow l + \text{hadronic cascade} \tag{2.45}$$

This lepton loses its energy continuously by ionisation processes and other stochastic processes like e.g. bremsstrahlung, pair production, nuclear interactions or Compton scattering. If the lepton moves faster than the speed of light in the surrounding medium, it emits a light cone, the so-called Cherenkov cone. The angle of Cherenkov light emission relative to the particle direction is described in Eq. (2.37). By this Cherenkov cone, the particle can be detected and its track can be determined. The parametrization of the mean angle between muon and neutrino Ψ is:

$$\Psi = 0.7 \cdot (\frac{E_\nu}{\text{TeV}})^{-0.7}. \tag{2.46}$$

From Eq. (2.46) it is possible to reconstruct the neutrino path from the lepton track [LM00].

2.4.5 Nuclear reactions

Nuclear reactions can take part only when a high energy proton or nucleus hits a nucleus almost directly as the strong force has only small range. In the case of a proton hitting a nucleus, the cross-section equals more or less the radius of the nucleus. An estimation of the radius is given by [Lon81b]

$$R = 1.2 \cdot 10^{-15} A^{1/3}\,\text{m}$$

where A is the mass number of the nucleus. More general, the cross-section for the interaction of two nuclei is described as

$$R = 1.2 \cdot 10^{-15} (A_1^{1/3} + A_2^{1/3})\,\text{m}$$

for two nuclei with mass numbers A_1 and A_2, respectively. The proton interacts with the individual nucleons within a nucleus. It also interacts with the nucleons along the line of flight, so the process can be considered as a proton undergoing multiple scattering inside the nucleus. There are some general "rules" for the interaction of high energy protons with nuclei:

- The proton reacts with an individual nucleon. In the interaction, mainly pions of all charges are produced, but also strange particles, and even anti-nucleons.
- In the reference frame, the pions emerge mainly in forward and backward directions.

- The nucleons and pions all possess very high forward motion in the laboratory frame of reference and hence come out with very high energy.

- As each of the secondary particles may also interact further, cascades may be produced inside of the nucleus.

- The nucleons taking part in the interaction are usually removed from the nucleus, leaving it in a highly excited state. The resulting nucleus does not need to be stable. If the resulting nucleus is unstable, it can happen that one or more nucleons evaporate, which is called spallation.

In the atmosphere, collisions of very high energetic incident cosmic ray nuclei with atoms of the atmospheric gas can lead to a stream of spallation products which are themselves able to start other nucleonic cascades.

2.4.6 Extensive air showers

When a high energy particle from space enters the atmosphere of the Earth, all of the processes described in the sections above happen in a cascading way leading to the phenomenon called "extensive" air showers. To study extensive air showers it is useful to have a look at the atmosphere which is the medium the interaction takes place in. The Earth's atmosphere has a total atmospheric depth of $X = 1030\,\mathrm{g/cm^2}$. The mass is distributed in the vertical as

$$\rho(h) = \rho_0 \exp(-h/H) \tag{2.47}$$

with the scale height $H \approx 7.5\,\mathrm{km}$. The atmospheric depth at altitude h is then

$$X(h) = X \exp(-h/H)$$

The mean free path in the atmosphere is with the density ρ, Avogadro number N_A, and m_A the molecular mass,

$$\lambda_I = \frac{m_A}{\rho N_A \sigma}$$

The interaction length is independent from the density:

$$\tilde{\lambda}_I \equiv \lambda_I \rho = \frac{m_A}{N_A \sigma}$$

Protons have an interaction length in air of $\lambda_I \approx 90\,\mathrm{g/cm^2}$, which means that the atmosphere has about 12 interaction lengths. The mean altitude of the first interaction can be calculated:

$$\tilde{\lambda} = X(h) = X \exp(-h/H) \Rightarrow h = H \ln \frac{X}{\tilde{\lambda}} \approx 16\,\mathrm{km}$$

In the atmosphere, protons or nuclei from cosmic radiation collide in-elastically with nuclei in the atmosphere undergoing strong interactions. In these interactions, pions are produced which themselves decay or interact.

$$\begin{aligned} \pi^0 &\longrightarrow 2\gamma \\ \pi^+ &\longrightarrow \mu^+ + \nu_\mu \\ \pi^- &\longrightarrow \mu^- + \bar{\nu}_\mu \end{aligned}$$

The π^0 decay in two γ's and generate the electromagnetic component of an air shower while the charged pions contribute to the muonic component. Electromagnetic interactions within the shower are mainly ionisation, Bremsstrahlung and pair production.

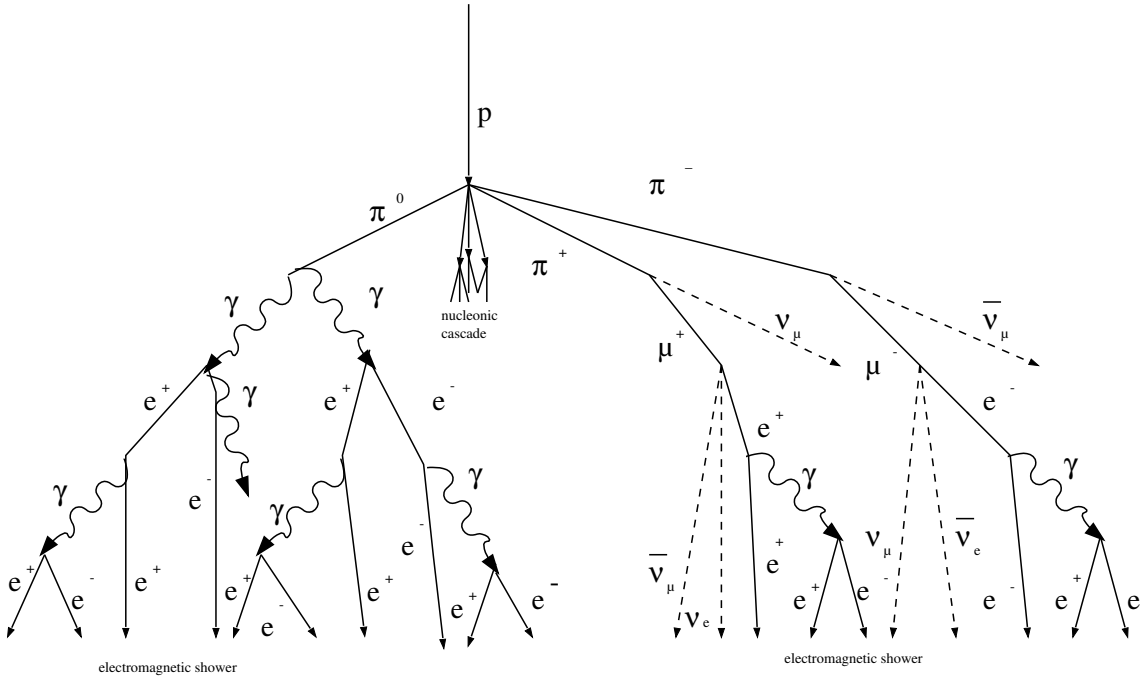

Figure 2.4: Scheme of an extensive air shower

In a simple model of an electromagnetic shower, the number of particles grows by a factor of two after each radiation length and the energy per particle is divided in half [Lon81b]. After

$$n = \frac{X(h)}{\tilde{\lambda}}$$

there are on average

$$N = 2^n = 2\frac{X(h)}{\tilde{\lambda}}$$

particles with an energy

$$E_n = \frac{E_0}{N}$$

in the shower. The shower develops until electrons reach their critical energy (E_{crit}). When the energy drops below E_{crit}, no more bremsstrahlung takes place and the further energy loss is by ionisation. In air, Nitrogen with $Z = 7$ is the most abundant molecule. Therefore, the critical energy

$$E_{crit} = \frac{710\,\mathrm{MeV}}{Z + 0.92},$$

in the atmosphere results $E_{crit} \simeq 100\,\mathrm{MeV}$. A purely electromagnetic shower can produce up to $N_{max} = E_0/E_{crit} = 10^{10}$ particles! Considering also hadronic processes this number drops to $\sim 10^9$. In the hadronic shower, the proton loses on average half of its energy in the first hadronic interaction. Protons also have a longer interaction length than heavier nuclei. The maximum of a shower generated by a heavy nucleus is therefore higher than for a proton induced shower. In general there are three components in a cosmic ray air shower (Fig. 2.4):

- electromagnetic component ($\gamma, \mathrm{e}^-, \mathrm{e}^+$)
- muonic component resulting from the decay of π's produced in hadronic interactions consisting of muons and neutrinos.
- hadronic component, consisting of e.g. protons, pions

2.5 Detection of cosmic rays

Depending on the primary particle energy, there are multiple ways to detect cosmic rays. With most methods, cosmic ray particles are detected in an indirect way. As cosmic ray primaries interact within the atmosphere, direct observation is only possible from stratosphere or space. Indirect measurements of low energy particles are carried out with ground-based. For the observation of high energy particles, indirect methods are necessary. As these particles are very rare, huge detector arrays are needed. Indirect measurements are therefore limited to the Earth surface.

2.5.1 Low energy particle detection methods

Ground-based detectors

For energies below the TeV range it is possible to measure the integral flux at the surface, but not the energy spectrum. There is a variety of means for detecting cosmic rays at the Earth's surface. A very common way is the use of scintillation counters with several layers to count coincidences. In this energy region detectors are mainly used to observe solar particles or the suppression of the flux of galactic cosmic rays due to the heliosphere. A world-wide web of neutron monitors observes the solar particle fluxes and the so called "space weather" [Sim00]. Such a detector is, for example, located in the high altitude research station at Jungfraujoch, Switzerland.

Airborne detectors

In 1912 Victor Hess demonstrated the existence of cosmic rays with balloon flights to more than 5700 m. On these altitudes cosmic ray primaries are measured mostly directly, using different detection techniques. Victor Hess used a simple Geiger counter. In modern times there is e.g. the BESS experiment[1]. BESS (the Balloon-borne Experiment with a Superconducting Spectrometer) flew at stratospheric depth and searched for anti-protons within the cosmic radiation [Noz04]. Another balloon-borne experiment is ISOMAX, with driftchamber, Cherenkov-detector and a time-of-flight detector it was designed to measure composition of cosmic radiation. There are many more balloon experiments, for an overview of NASA balloon activities see [I+05].

Spaceborne detectors

The field of space missions for cosmic ray research is large. There are missions observing the Sun and measuring solar wind particles and solar cosmic rays, e.g. Ulysses, SOHO, Wind and others. Especially interesting in the field of cosmic ray research are the PAMELA[2] and AMS[3] missions. The PAMELA (Payload for Antimatter Matter Exploration and Light Nuclei Astrophysics) [PSP10] is equipped with a time-of-flight detector, a magnetic spectrometer, several layers of plastic scintillator, calorimeter and a neutron detector and was designed to measure the composition and the energy spectra of electrons, positrons, anti-protons and light nuclei. PAMELA is still on an Earth orbit installed on a Russian satellite.

AMS, the Alpha Magnetic Spectrometer Experiment [Amb03] is equipped with instruments to measure cosmic ray composition and flux. AMS-01 was the first version, flying on the Space Shuttle, while AMS-02 started operation on the International Space Station (ISS) recently.

2.5.2 High energy detection methods

When particle energies exceed $\sim 100\,\mathrm{TeV}$, the flux drops below one particle per square meter per year. Direct measurements would take too much time until yielding reasonable statistics there. For these cases indirect measurements are chosen.

Air shower arrays

Air shower arrays consist of large numbers of ground stations spread over a wide area. Not the primary particle itself is measured but the amount of energy of the secondaries produced by the interaction of the cosmic ray primary with nuclei in the atmosphere. The stations consist mainly of scintillator or water or ice Cherenkov detectors. The largest detector field so far belongs to the Pierre Auger Observatory in Argentina [AAA+04]. Water Cherenkov-detectors detect charged particles emitting Cherenkov-radiation inside

[1] http://www.universe.nasa.gov/astroparticles/programs/bess/
[2] http://pamela.roma2.infn.it/
[3] http://www.ams02.org/

the tank. The maximum energy of the primary particle which can be measured does not depend from one tank but from the number and the area they are spread on.

Figure 2.5: Air shower array (Tibet) [col03]

Fluorescence telescopes

When a charged particle interacts with atmospheric nitrogen latter is excited to a higher state falling back by emitting ultraviolet light. This process is called fluorescence. Fluorescence telescopes like e.g. Flys eye or the telescopes around the ground field of the Pierre Auger Observatory can detect the emitted UV light. With the Air-Fluorescence technique air showers can be observed up to the highest energies [AAA+10].

Cherenkov telescopes

The Cherenkov principle [Lor99] is not only used in water or ice tanks at ground stations, also in the atmosphere, a charged particle can emit Cherenkov radiation. Air-Cherenkov-Telescopes are used e.g. in the H.E.S.S.-Experiment in the desert of Namibia, or MAGIC on the canary island of La Palma. Air-Cherenkov-Telescopes mainly measure very high-energy gamma rays. Telescopes working with the Fluorescence- or Imaging Air Cherenkov Technique can only be operated in moon- and cloudless nights.

Figure 2.6: Air-Cherenkov telescopes in the Namibian desert [col05]

Chapter 3

Anisotropy

Studying cosmic ray anisotropy can provide information on origin, composition and propagation of cosmic rays, but also on drifts and diffusion in the galaxy as well as about galactic magnetic fields.

An anisotropy A can be expressed as

$$A = \frac{I_{max} - I_{min}}{I_{max} + I_{min}}. \tag{3.1}$$

With I_{max} and I_{min} as maximal and minimal intensity. The equation Eq.(3.1) can be solved by multi-pole development. The solution for a single maximum in first order approximation considering only one direction would look like:

$$I(\alpha) = \bar{I} + \vartheta \bar{I} \cos(\alpha - \phi) \tag{3.2}$$

where $\bar{I}$ is the mean intensity, α the right ascension, and ϑ and ϕ the anisotropy parameters amplitude and phase, respectively [Mol09]. Within the diffusion model, the amplitude ϑ is also linked to the diffusion coefficient D as [PJSS05]

$$\vartheta = \frac{3D\nabla I}{cI}. \tag{3.3}$$

3.1 Anisotropies at low energies ($< 100\,\mathrm{GeV}$)

In this low energy region, the flux is dramatically influenced by the solar activity. Most anisotropies result from the interaction of low energy cosmic ray particles in the heliomagnetic field, see [Pot13].

3.1.1 Anisotropies caused by the Sun

Daily variations

Cosmic ray flux at the Earth's surface is highly depending on atmospheric parameters like pressure or temperature. Flux is then correlated with the pressure-variation between day and night.

27-day-cycle

Cosmic ray flux anomalies may be observed at mean intervals of 27 days. This quasi-periodic recurrence of certain effects is a well known phenomenon and is linked to the 27-day rotational period of the Sun. Frequently, it is related to sunspot activity or co-rotating interaction regions.

11- and 22-year cycle (solar modulation)

As low energetic cosmic rays penetrate the heliosphere, they are influenced by the solar wind. This influence can be seen in intensity variations that are caused by solar activity and are referred to as "solar modulation effects". An intensity variation has been found with a period of 11 years. This period is equivalent to the 11-year solar cycle and is anti-correlated with the solar activity. On top, a variation occurs with a period of 22 years. This is linked to the polarity reversal of the heliospheric magnetic field.

Non-periodic effects

Effects like Forbush decrease (FD), ground-level enhancement (GLE), electric storm particles (ESP), and others, are highly aperiodic and unpredictable. They are usually correlated with strong solar flares or coronal mass ejections. The frequency of these events is correlated with the solar activity cycle.

See [Flü01] and references therein. All these effects lead to highly unpredictable, local anisotropies which will not be discussed further within this work.

3.2 Anisotropies at energies $> 100\,\mathrm{GeV}$

Starting at this energy, the Sun has nearly no influence on the particle flux any more. Large scale anisotropy signals from drifts and diffusion and from the motion of the Earth within the galaxy are to be expected. Due to the deflection of charged particles, a more isotropic flux is expected with some intermediate scale clustering when rising the observed energy even higher. At the highest energy, deflection is small and the GZK-horizon limits the distance from the sources. Only small scale clustering is expected [Mol09].

3.2.1 NFJ-Model

The NFJ-Model, proposed by Nagashima-Fujimoto-Jacklyn [NFJ98], explains cosmic ray anisotropies measured by several ground based detectors around the world in the energy region $\sim 10^3 - 10^4\,\mathrm{GeV}$ through the existence of two superposed anisotropies, a galactic one and one supposed to be of heliospheric origin. The galactic anisotropy from direction $\alpha = 0\,\mathrm{h}$, $\delta = -20°$ is described by its deficit flux confined in a narrow cone with half opening angle $\chi_G = 57°$ at right ascension $\alpha_G = 12\,\mathrm{h}$ and declination $\delta_G = 20°$. It is visible in a broad energy range from about $60\,\mathrm{GeV}$ to $10^4\,\mathrm{GeV}$ and higher.

The second anisotropy confines an excess flux in a cone with half opening angle estimated to $\chi_T = 68°$ from the direction $\alpha_T = 6\,\mathrm{h}$ and $\delta_T = -24°$. It is called "tail-in" because its direction coincides somehow with the expected direction of the heliomagnetotail, opposite the proper motion. It is visible only at small energies with a maximum at $10^3\,\mathrm{GeV}$ and vanishes above $10^4\,\mathrm{GeV}$. Most likely it is from heliospheric origin rather than galactic.

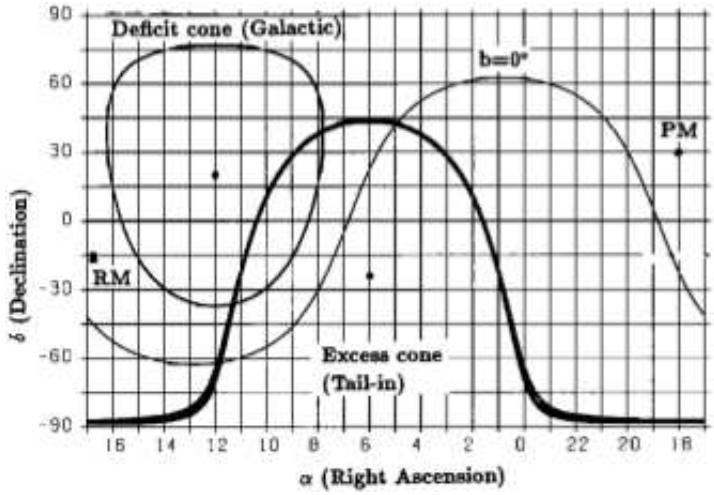

Figure 3.1: The galactic and the heliotail-in anisotropies. The $b = 0°$-line indicates the galactic equator. In the upper left, the thin line borders the deficit cone of the galactic anisotropy, the thick line in the middle the excess cone of the tail-in anisotropy [NFJ98]

Fig. 3.1 shows both anisotropies, the galactic one with its deficit flux in the upper left, and the tail-in excess flux in the lower middle, confined by the thick line. $b = 0°$ marks the galactic equator. The response to the flux is maximum in December solstice, when Earth is closest to the heliomagnetic tail and reaches a minimum in June solstice when the Earth is far-est away from the heliomagnetic tail. The NFJ-Model seems to fit quite well the data of e.g. the Super-Kamiokande experiment [GHI+05] and it can explain the strange north-south-asymmetry which has been observed by telescopes with the energy range in the transition from low to high energy, but it does not support the Compton-Getting-effect [CG35].

3.2.2 Compton-Getting-Effect

In 1935, A. H. Compton and I. A. Getting postulated "An Apparent Effect of Galactic Rotation on the Intensity of Cosmic rays" [CG35], which treats the possibility of a cosmic ray anisotropy due to the motion of the Earth within the galaxy. This motion is estimated to be $\approx 300\,\mathrm{km/s}$ in the direction of $\alpha = 20\,\mathrm{h}40\,\mathrm{min}$ and $\delta = 47°$. Cosmic rays were assumed to origin mostly from outside the galaxy, moving in its rest frame. If the remote galaxies move with velocities around $\approx 80\,\mathrm{km/s}$, this means that the relative

motion of the Earth and assumed cosmic ray sources would approximately correspond to the velocity of the galactic rotation. This would affect the number density of cosmic rays as well as the intensity.

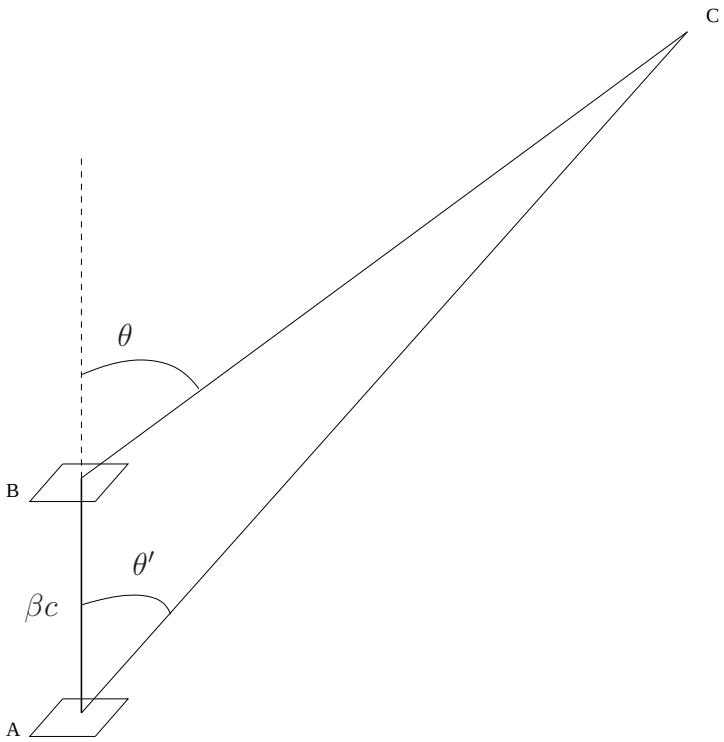

Figure 3.2: Illustration of the relative movement of the systems [CG35].

In Fig. 3.2, A is a surface moving with the velocity βc (with $\beta \ll 1$) towards B. C is the cosmic ray source. Assuming a constant number of particles per unit path, the number of particles hitting the stationary surface B is

$$n = (1 - \beta \cos\theta) \cdot \cos\theta \cdot 2\pi \sin\theta \mathrm{d}\theta. \tag{3.4}$$

While in the same interval the moving surface A is hit by

$$n' = 1 \cdot \cos\theta' \cot 2\pi \sin\theta \mathrm{d}\theta \tag{3.5}$$

particles. This results in an increase of the number density of

$$\frac{n'}{n} = \frac{1}{(1 - \beta \cos\theta)^3}, \tag{3.6}$$

as well as an increase in intensity of

$$\frac{I'}{I} = \frac{1}{(1 - \beta \cos\theta)^4}. \tag{3.7}$$

Amplitude and phase have been predicted to 0.05% and 20 h 40 min respectively. On the basis from data collected by high altitude ionisation chambers the analysis of the first harmonic yields an amplitude of 0.043±0.0045% With a maximum at 21 h31 min±23 min. This result would imply that a considerable part of the cosmic radiation origins from outside the galaxy [CG35].

Problems:

- The energy region is not specified.
- Transition from galactic to extragalactic cosmic rays does probably not happen until very high energy.
- It is not clear if cosmic rays indeed move with the rotation of the galaxy.
- The energy of particles which can be measured in a ionisation chamber will probably not reach the energy region where the transition is assumed to take place.

Later, the bulk of cosmic rays is assumed to originate from inside the galaxy. The Compton-Getting-Effect is adopted for galactic cosmic rays moving within a reference frame fixed to the interstellar medium. There, the motion of the Earth changes to the individual velocity of the Sun and the heliosphere relative to the interstellar medium which is $\approx 21\,\mathrm{km/s}$. The amplitude resulting from this assumption has been calculated to be 0.03% e.g. by [GA68] (see also references therein).

The anisotropy can also be calculated for the solar modulation at energies below $\approx 10\,\mathrm{GeV}$. The moving plane is then the Earth around the Sun with a velocity of 29.8 km/s. The maximum of this anisotropy appears at 6 h with an amplitude depending from the geographical latitude up to $\simeq 5 \cdot 10^{-3}$ [Mol09].

Cosmological Compton-Getting-Effect

On cosmological scale, the cosmic rays are isotropic in the rest frame of the cosmic microwave background (CMB), and the Earth is moving with the galaxy with a velocity of $\approx 370\,\mathrm{km/s}$. For these values, [GA68] predicted an anisotropy amplitude of 0.6%. For ultra high energy cosmic rays (UHECR, $E > 10^{18}\,\mathrm{eV}$), the study of the Cosmological Compton-Getting-Effect (CCGE) can provide lots of information on topics like e.g. the composition, the origin, the transition from GCR to EGCR, or galactic magnetic fields (GMF). Nowadays two models exist for the ankle in the cosmic ray spectrum. In one, the cross-over of the steep end of the spectrum of galactic cosmic rays and the flatter extragalactic flux is responsible for change in the power-law index, while the other interprets the ankle as a dip due to energy loss by $e^- - e^+$ pair production of cosmic ray primaries with the CMB [BGG05].

Some properties of the CCGE are be [KS06]:

- The amplitude should be independent from energy and charge.
- The magnitude of the amplitude should be independent from deflection of UHECRs within the GMF.

- The dipole vector and -position should not be far away from the CMB ones.
- It provides information about the transition of GCR to EGCR: Going to lower energies, it should decrease and be replaced by the galactic anisotropies.
- At even higher energy it is expected that the CCG vanishes and is replaced by local inhomogeneities.

Problems: There is yet a lack of statistics for particles with $E > 10^{18}\,\mathrm{eV}$ and higher. Results about the search for cosmic ray anisotropies at ultra high energies are presented e. g. in [Pie12].

3.2.3 Stochastic supernova explosions

Is the anisotropy in the energy region from tens of GeV to sub-PeV measured so far simply an effect of the stochastic character of supernova explosions? In [EW06] another anisotropy model is presented: Studying the effects of the stochastic character of supernova explosions on the iso- or anisotropy of cosmic rays below the knee. It is widely accepted, that cosmic rays below the knee are produced and/or accelerated within the shocks of supernova explosions. 10^6 random distributed SN explosions, uniformly distributed in time corresponding to a rate of explosions of Type II SN of 10^{-2} per year are simulated, the shocks and accelerated particles within are then propagated through the interstellar medium (ISM). Some results presented in the paper show surprising correlation with experiments. The simulations show, that it is in principle possible for the anisotropy measured so far to result from the stochastic character of supernova explosions.

3.3 Analysis methods

3.3.1 Classical analysis

As seen in the section before, one anisotropy signal which can probably be expected is a dipole. For a start, the intensity and amplitude shall be defined. The intensity I may be defined as the number of particles passing through a unit area perpendicular to the direction of observation $\boldsymbol{u}$ per unit time and solid angle, and the amplitude as

$$A = \frac{I_{max} - I_{min}}{I_{max} + I_{min}}. \tag{3.8}$$

In the most classical way, a Rayleigh analysis is performed in the right ascension. The k-order harmonic amplitude for N events with the right ascension α_i is

$$r_k = \sqrt{a_k^2 + b_k^2}, \tag{3.9}$$

and the phase

$$\phi_k = \arctan\left(\frac{b_k}{a_k}\right) \tag{3.10}$$

with

$$a_k = \left(\frac{2}{N}\right) \sum_i^N \cos(k\alpha_i) \qquad \text{and} \qquad b_k = \left(\frac{2}{N}\right) \sum_i^N \sin(k\alpha_i).$$

The probability that an amplitude $r \geq r_k$ arises from an isotropic sample, can be estimated to $P(\geq r_k) = \exp(-Nr_k^2/4)$.

Following the central limit theorem [DM38], the a_k and b_k have a Gaussian distribution with $\langle a_k^2 \rangle = \langle b_k^2 \rangle = 0$ and $\sigma^2(a_k) = \sigma^2(b_k) = \frac{2}{N}$.

The probability of finding the amplitude larger than r_k in a amplitude interval from r_k to $(r_k + \mathrm{d}r_k)$ is then given by the integral

$$P(\geq r_k) = \frac{1}{2} \int_{r_k}^{r_k + \mathrm{d}r_k} \exp\left(-\frac{Nr_k^2}{4}\right) N r_k \mathrm{d}r_k \tag{3.11}$$

[Mol09]. The Rayleigh procedure brings information on the projection of the dipole in the equatorial plane.

3.3.2 East-West-Analysis

The East-West method was first proposed by [Lin75] and was later reviewed in [BAD+11]. It is an exposure-independent method for the search for cosmic ray anisotropy with large detectors, e.g. cosmic ray air shower arrays. It is aimed to determine the dipole anisotropy just by counting rates in two sectors of a detector. Cosmic rays, as they travel downward to the detector, are influenced by different kind of effects. Such can be experimental effects like changing of measurement conditions during data taking, or atmospheric effects.

In the East-West method, counting rates from two sectors of the detector ("East" and "West") are subtracted from each other. A harmonic analysis on the difference is then correlated with the first derivative of the cosmic ray intensity. If there is a real dipole, as the Earth rotates Eastward, the Eastern sky is closer to the dipole excess region for half a day. The other half of the day, the Western sky is closer to the excess region and shows higher counting rates. Therefore there is some kind of oscillation in the difference between East and West sector whose amplitude and phase is expected to be correlated with the real dipole.

In principle, the East-West-method is based on the assumption that the difference between the observed counting rates during one sidereal day in the Eastern and the Western hemisphere ($I_E^{obs}(t)$ and $I_W^{obs}(t)$) is proportional to the first derivative of the true total counting rate (I_{tot}^{true}), in the classical approach the proportionality coefficient being the mean hour angle $\langle h \rangle = \int_{\delta_{min}}^{\delta_{max}} \mathrm{d}\delta \cos\delta \int_{t-\pi}^{t} \mathrm{d}\alpha \omega(t-\alpha, \delta)(t-\alpha)$:

$$I_E^{obs}(t) - I_W^{obs}(t) \simeq \langle h \rangle \frac{\mathrm{d}I_{tot}^{true}}{\mathrm{d}t} \tag{3.12}$$

The classical approach holds for experiments at geographical latitudes between $-50°$ and $50°$. For a more detailed calculation see [BAD+11]. A harmonic analysis is then

performed on the difference of the counting rates $I_E^{obs}(t) - I_W^{obs}(t)$, which, as seen before, equates more or less $\frac{\mathrm{d}I_{tot}^{true}}{\mathrm{d}t}$. The coefficients for the harmonic analysis have to be slightly corrected for the subtraction to become:

$$a = \frac{2}{N}\sum_{i=1}^{N}\cos(t_i+\zeta_i), \qquad \text{and} \tag{3.13}$$

$$b = \frac{2}{N}\sum_{i=1}^{N}\sin(t_i+\zeta_i). \tag{3.14}$$

In Eq.(3.13) and Eq.(3.14), ζ is a variable with the value 0 if the event is coming from the East side, and π if coming from West side. From Eq.(3.14), amplitude and phase of $\frac{\mathrm{d}I_{tot}^{true}}{\mathrm{d}t}$ can then be estimated to:

$$\hat{r} = \frac{\pi\cos\ell}{2}\frac{\langle\cos\theta\rangle}{\langle\sin\theta\rangle}\sqrt{a^2+b^2} \tag{3.15}$$

and

$$\hat{\phi} = \arctan\left(\frac{b}{a}\right) \tag{3.16}$$

respectively. (In Eq.(3.15) and Eq.(3.16), ℓ is the geographic latitude of the detector and (φ,θ) the local coordinates of the viewing direction) For amplitude and phase of the intensity itself, $\frac{\mathrm{d}I_{tot}^{true}}{\mathrm{d}t}$ has to be integrated. $\hat{r}$ and $\hat{\phi}$ can then be estimated to

$$\hat{r}_I = \frac{N}{2\pi}\hat{r} \qquad \text{and} \qquad \hat{\phi}_I = \hat{\phi}+\frac{\pi}{2}. \tag{3.17}$$

In the standard Rayleigh analysis, the dipole amplitude and phase is related to the first harmonic amplitude as follows:

$$r_{RA} = \left|\frac{\langle\cos\delta\rangle D_\perp}{1+\langle\sin\delta\rangle D_\parallel}\right| \tag{3.18}$$

where $D_\parallel = D\sin\delta_d$ is the component of the dipole along the Earth rotation while $D_\perp = D\cos\delta_d$ is the dipole component in the equatorial plane.

The relation of the amplitude and phase reconstructed with the East-West method with the first harmonic amplitude and phase of the dipole $(\hat{D}_\perp, \hat{\phi}_d)$ is

$$\hat{D}_\perp = \langle\cos\delta\sin h\rangle\sqrt{a^2+b^2} \tag{3.19}$$

and

$$\hat{\phi}_d = \arctan\left(\frac{b}{a}\right)+\frac{\pi}{2}, \tag{3.20}$$

respectively.

The East-West method may be less sensitive, but in many cases it can help a lot because it rules out unknown effects of the detector and turns corrections on counting rates for atmospheric effects needless.

3.3.3 Forward-Backward-Asymmetry method

The Forward-Backward-Asymmetry analysis [AAA+09] is another method for the search for anisotropy within the arrival directions of cosmic rays. In the Forward-Backward-Asymmetry (FB) method, count rates (N_F and N_B) are taken in a small time interval in two regions of the detector within a small but equal solid angle. It is based on the equation

$$FB = \frac{N_F - N_B}{N_F + N_B} \tag{3.21}$$

The method uses the rotation of the Earth and searches for a coherent modulation in the Forward-Backward-Asymmetry. This modulation, if found, is a function of the anisotropy. If an excess region in the sky is passed by the telescope, it first fills the forward looking part, making the FB value more positive, then fills the backward looking part which leads to higher count rates there and so there is an oscillation. The FB-method is closely related to the EW-method. But while the EW-method can be thought of one integrated measurement, the FB-method uses multiple localised and independent measurements. Instrumental or weather effects are averaged out by summing many full days. This results in the suppression of random signals but not of a coherent one. The method measures the modulation in the direction of the Earth's rotation so it cannot yield any information on the modulation in the declination. To create a full 2D map of the sky, small zenith bands have to be evaluated independently. For the analysis it is assumed that the anisotropy signals in each declination band can be described with a Fourier series and that they are small with respect to the isotropic flux.

3.4 Analysis and results from other experiments

Anisotropy studies have been carried out by a number of experiments with different results. Here follows a compilation of these studies.

- KASCADE [AAB+04]
  KASCADE is located in Karlsruhe, Germany, at 49.1° N, 8.4° E, 110 m above sea level. It consists of central detector, a muon tracking detector, and a large field array to measure hadronic, muonic and electromagnetic components of extensive air showers in the energy region around the knee. With a rate of $\sim 3\,\mathrm{Hz}$, 10^8 air showers were collected in the energy range $0.7 - 6\,\mathrm{PeV}$ and, after careful stability checks, used in the analysis. The data was taken during 1600 days of detector lifetime between May 1998 and October 2002.

  Result

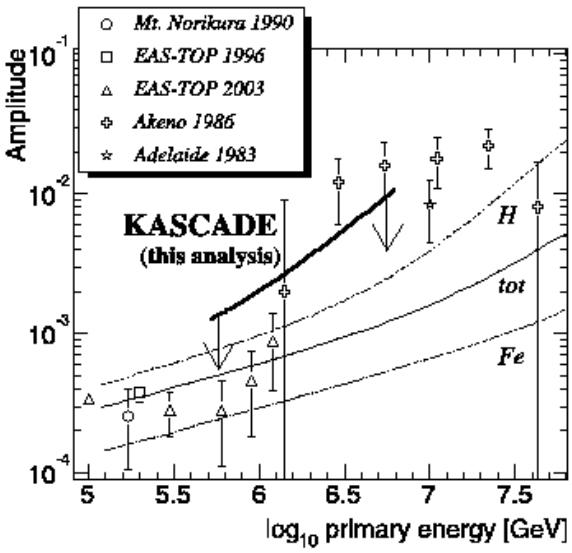

Figure 3.3: Limit on anisotropy amplitude from KASCADE [AAB+04]

The KASCADE analysis on large scale anisotropies led to an upper limit on the amplitude. Fig. 3.3 shows these limits vs. energy of the primary particle compared to other experiments (see legend) and theoretical predictions for proton, iron and total flux.

- Super-Kamiokande [GHI+05]
  Super-Kamiokande is a huge tank filled with 50000 tons of pure water and instrumented with 13031 photomultiplier in total. It is located 1000m underground in the Kamioka mine in the Gifu Prefecture, Japan. Its latitude and longitude are 36°25′ N and 137°18′ E, respectively. Super-Kamiokande records cosmic ray muons with a rate of $\sim 1.77\,\mathrm{Hz}$. Sheltered by the rock overburden of 2400 m.w.e., only muons with more than $\sim 1\,\mathrm{TeV}$ at ground level can reach the detector. The main purpose of the detector is neutrino physics with atmospheric and solar neutrinos. Super-Kamiokande is sensitive on primary cosmic rays with a median energy of 10 TeV. The data set used for the anisotropy analysis was recorded between June 1, 1996 and May 31, 2001. During this period, a total of $2.54 \cdot 10^8$ cosmic ray muons were collected. $2.10 \cdot 10^8$ of them entered in the analysis.

  Result
  Super-Kamiokande reported an excess flux in direction of Taurus and a deficit flux in direction of Virgo. Fig. 3.4, (a) shows the fractional deviation from the isotropic, (b) the standard deviation. The red and blue lines show the Taurus excess and Virgo deficit, respectively. The amplitude is found to be $(1.04 \pm 0.20) \cdot 10^{-4}$ for Taurus excess and $-(0.94 \pm 0.14) \cdot 10^{-3}$ for Virgo deficit. This result seems to fit very well in the NFJ-model, but it gives no evidence for the Compton-Getting-effect.

- Tibet AS-γ [AAB+06]

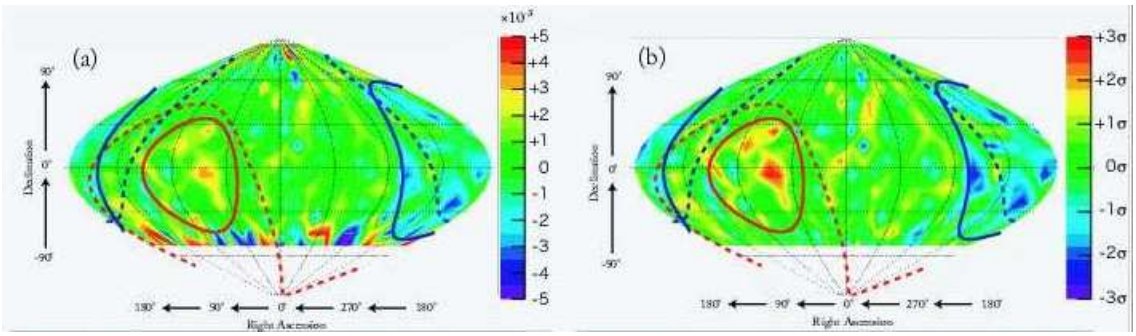

Figure 3.4: Sky plot from Super-Kamiokande [GHI+05]

The Tibet AS-γ experiment is an air shower array consisting of 733 plastic scintillator spaced in 7.5 m and 15 m and is located in 4300m above sea level at 90.53° E, 30.11° N in Tibet, China. The energy threshold of the detector is 7 TeV, which is remarkably low for such an experiment. The data used in the analysis was collected between February 1997 to September 1999 during 555.9 days of lifetime with a rate of $\sim$ 105 Hz, and with an extended array at a rate $\sim$ 680 Hz during 1318.9 days of lifetime between November 1999 and October 2005. A total of $\sim 37 \cdot 10^9$ events were used in the anisotropy analysis.

Result

Fig. 3.5 shows relative CR intensity maps for the energies 4 TeV (A), 6.2 TeV (B), 12 TeV (C), 50 TeV (D), and 300 TeV (E), respectively. The Tibet analysis revealed besides the known tail-in excess and loss-cone deficit a slight excess in the Cygnus region ($\delta \sim 38°$ N, $\alpha \sim 309°$). It also shows the energy dependence of the anisotropies. Below 12 TeV (A to C), the energy dependence is not significant. At higher energies the anisotropy vanishes.

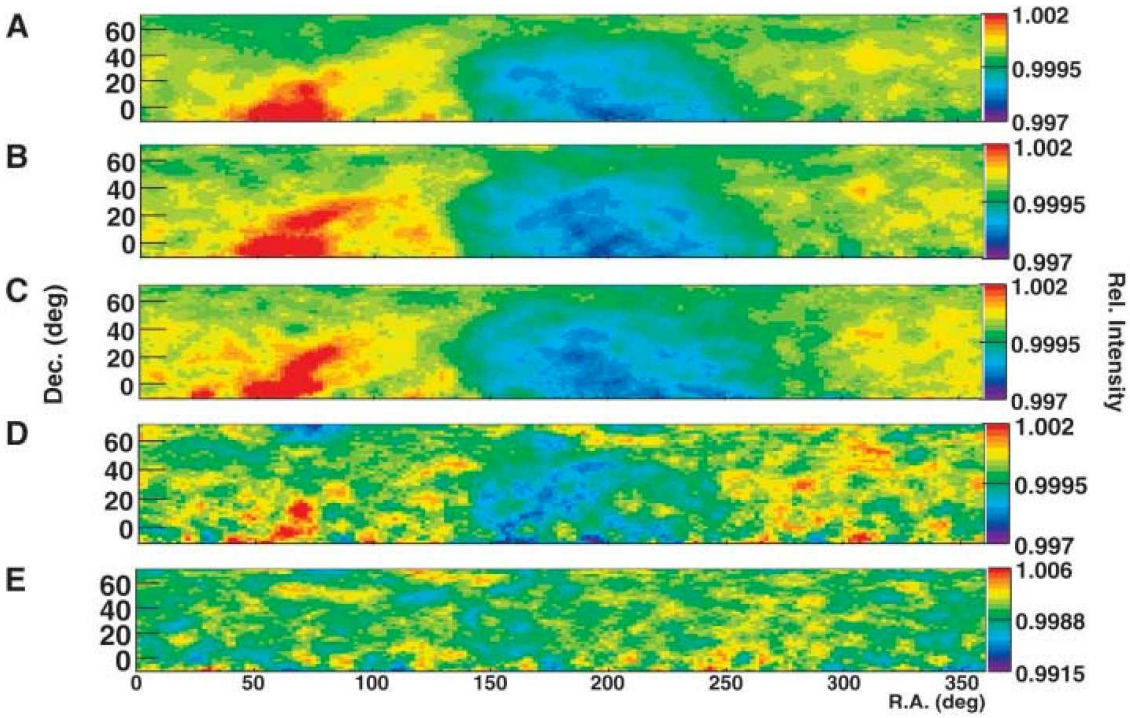

Figure 3.5: Results from the Tibet ASγ anisotropy analysis [AAB+06]

- IceCube [Abb12]
  IceCube is the successor of AMANDA at the South Pole. It is a neutrino telescope consisting of 86 strings with digital optical modules regularly spaced by 125 m over an area of approximately one square kilometre. The optical modules are buried 1.4 km to 2.4 km deep in the south polar ice.

  Result
  The IceCube result shows a good agreement with northern hemisphere detectors. As IceCube is placed at the same location as AMANDA, a comparison of these results is especially interesting. This will be shown in section 7.1.

3.4.1 Amplitudes and phases

Tab. 3.1 shows an overview of the obtained amplitudes and phases from other experiments.

Experiment	Energy	$A_{1sid}(10^{-4})$	ϕ_{1sid}	Year
SK	$\sim 10\,\mathrm{TeV}$	5.3 ± 1.0	$40° \pm 10$	1996-2001
Tibet AS-γ	$> 3\,\mathrm{TeV}$	3.2 ± 2.6	$253.9° \pm 46.5$	1997-2005
Milagro	$4 - 7\,\mathrm{TeV}$	4.0 ± 0.07	$104.3° \pm 0.5$	2000-2007
IceCube	$14\,\mathrm{TeV}$	6.4 ± 0.2	$66.4° \pm 2.6$	2007-2008

Table 3.1: Amplitudes and phases of the first harmonic as measured by other experiments [GHI+05, AAB+06, AAA+09, Abb10]

Chapter 4

The Antarctic Muon And Neutrino Detector Array(AMANDA)

4.1 Detection principle

While photons are absorbed and charged particles deflected by magnetic fields, the neutrino is, due to its small reaction cross-section, very penetrating. This makes it difficult to detect and very large detector volumes are needed for neutrino measurements. AMANDA, the Antarctic Muon And Neutrino Detector Array, is a detector array consisting of strings of optical modules - photomultiplier tubes sealed in glass pressure vessels - frozen in in the thick ice shelf close to the geographic South pole. The very pure ice serves as both, as neutrino target and Cherenkov medium. AMANDA was designed to search for neutrinos by looking downwards for Cherenkov light emitted by upward travelling muons from charged-current muon-neutrino interactions, using the Earth as shielding against muons from cosmic ray air showers [AAB+00]. But it can also be used to detect downward travelling muons and neutrinos resulting from cosmic ray interactions in the atmosphere.

The main channel for the production of these atmospheric muons and neutrinos is the interaction of the primary cosmic ray with nuclei in the atmosphere, producing pions of all charges. While neutral pions decays in photons, charged pions decay in muons and anti-muons. The muons resulting from these interactions cannot pass the Earth, so the Earth is used as shielding. This study is not about neutrino physics but about cosmic rays, therefore it is based on these usually rejected background data.

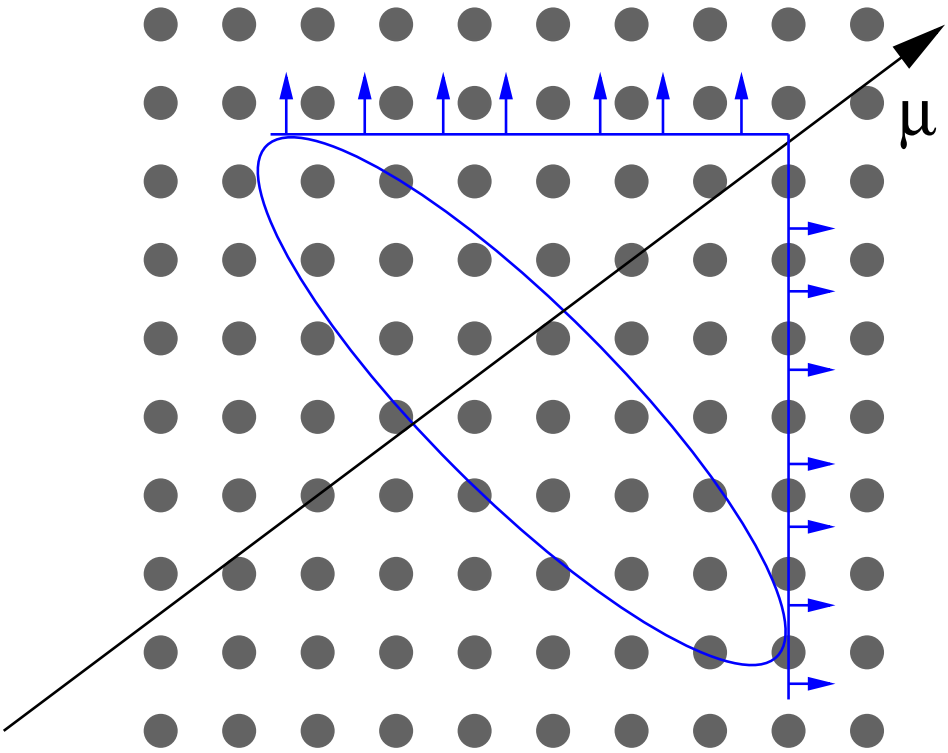

Figure 4.1: Sketch of the detection principle in a neutrino telescope[Wag04]

Fig.4.1 illustrates the detection principle for this kind of neutrino telescopes. A muon resulting from charged-current interactions of neutrinos in the ice or in the atmosphere travels through the instrumented area of the detector. On the track it emits Cherenkov-photons in a cone. The opening angle of this cone is, for relativistic tracks, $\sim 41°$. The Cherenkov-photons emitted along the track trigger the photo tubes in the optical modules. The muon track can then be reconstructed through the arrival times of photons in the OMs along track.

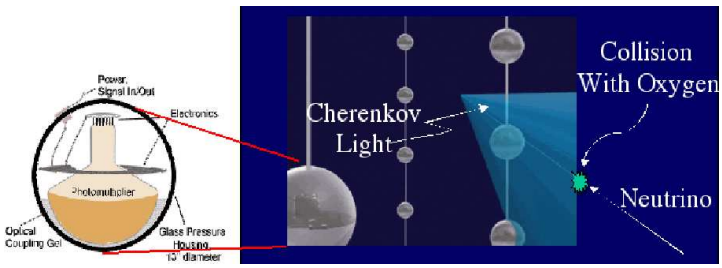

Figure 4.2: Optical module

4.2 AMANDA Setup

Figure 4.3: Panoramic view of the AMANDA site.

In 1988, Francis Halzen and John Learned presented their idea of a "solid state DUMAND" [HL88]. Instead of water, the detection body would consist of ice. As the ice in the South Polar cap is known to be very clear, they proposed Antarctica as location. In order to avoid the need for building a new station, the new neutrino telescope was decided to be built close to the USA's Amundsen-Scott-Station, located at the geographical South Pole. The construction started with the deployment of a prototype string in the 1991/1992 season and has been carried out in stages over the entire decade of the 1990's during the austral summer seasons as the South Pole station is not accessible during winter. The different stages of the construction are shown in Fig. 4.4 [AAB+00].

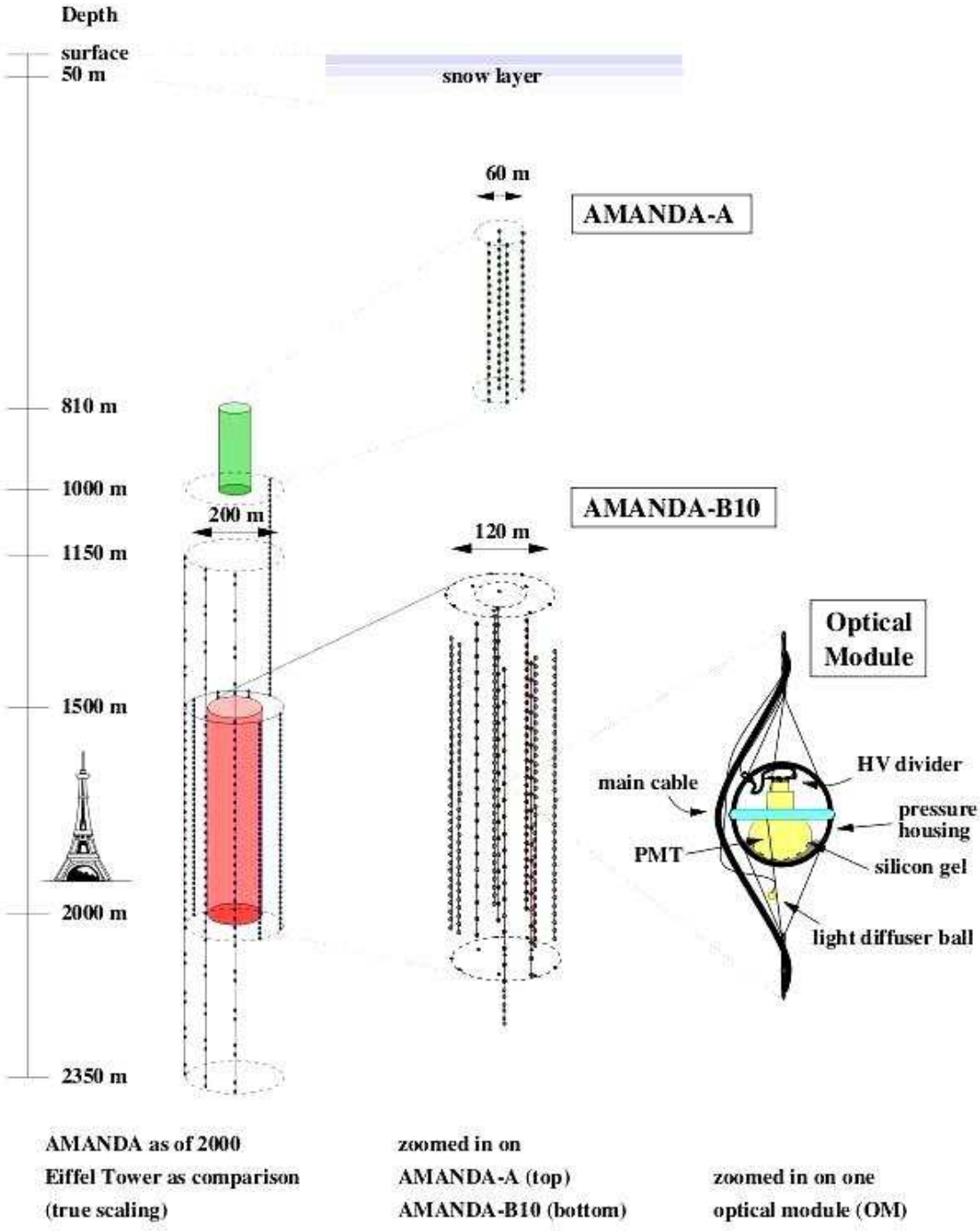

Figure 4.4: The different stages of AMANDA (A, B4, B10, II). Eiffel tower for size comparison (true scaling).[AAB+99]

4.2.1 History

Stage 1: AMANDA-A

In Antarctic summer 1993/1994, four strings were deployed near the geographical South Pole, in a depth of $800 - 1000\,\mathrm{m}$, to carry out studies of the optical properties of the ice. These studies revealed that a high concentration of air bubbles at these depths lead to large scattering, making accurate track reconstruction impossible. It could be used as calorimeter for energy measurements of neutrino-induced cascade-like events or as supernova monitor instead [MBP+94].

Stage 2: AMANDA-B4

With the lessons learned from AMANDA-A, a deeper array of 80 OMs on 4 strings was deployed at depths from $1500\,\mathrm{m} - 2000\,\mathrm{m}$, in the 1995/1996 season, forming the AMANDA-B4 prototype. Three AMANDA-B4 strings form a triangle of side length 61 m, 67 m, and 78 m, the fourth is located inside this triangle close to the centre [Hun99].

Stage 3: AMANDA-B10

During the 1996/1997 pole season, AMANDA-B4 was augmented by 6 additional strings to form the AMANDA-B10 detector. In this configuration, the detector consisted of 302 OMs on 10 strings. These strings are arranged in two concentric circles. The outer one has 6 strings on a diameter of 120 m, three other strings form the inner circle with a diameter of 60 m, one string is positioned close to the centre of the two circles [AAB+99].

Final stage: AMANDA-II

During the following two seasons, 9 additional strings were deployed forming a circle of 200 m in diameter around the AMANDA-B10 strings. In this final configuration, the AMANDA-detector consists of 19 strings with in total 677 optical modules, instrumenting a volume of $3000000\,\mathrm{m}^3$ of clearest polar ice to be both, target and Cherenkov medium. Final layout of the strings within AMANDA-II is shown in Fig. 4.5.

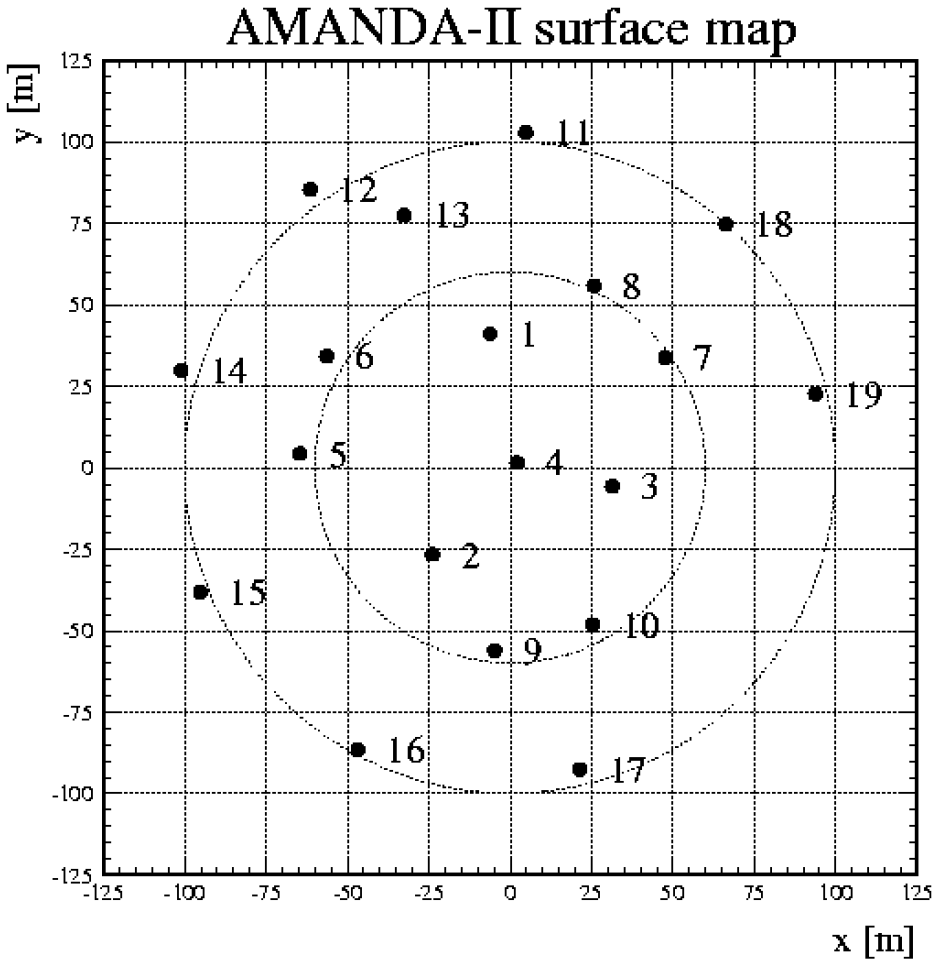

Figure 4.5: Detector layout from above [Sem06]

4.2.2 Instrumentation

The vertical spacing of the optical modules is 10 m or 20 m. Each OM consists of a pressure vessel of glass housing a photomultiplier tube (PMT). In order to reduce reflection in the glass, the PMT is mechanically and optically in contact with the glass sphere by a silicon gel.

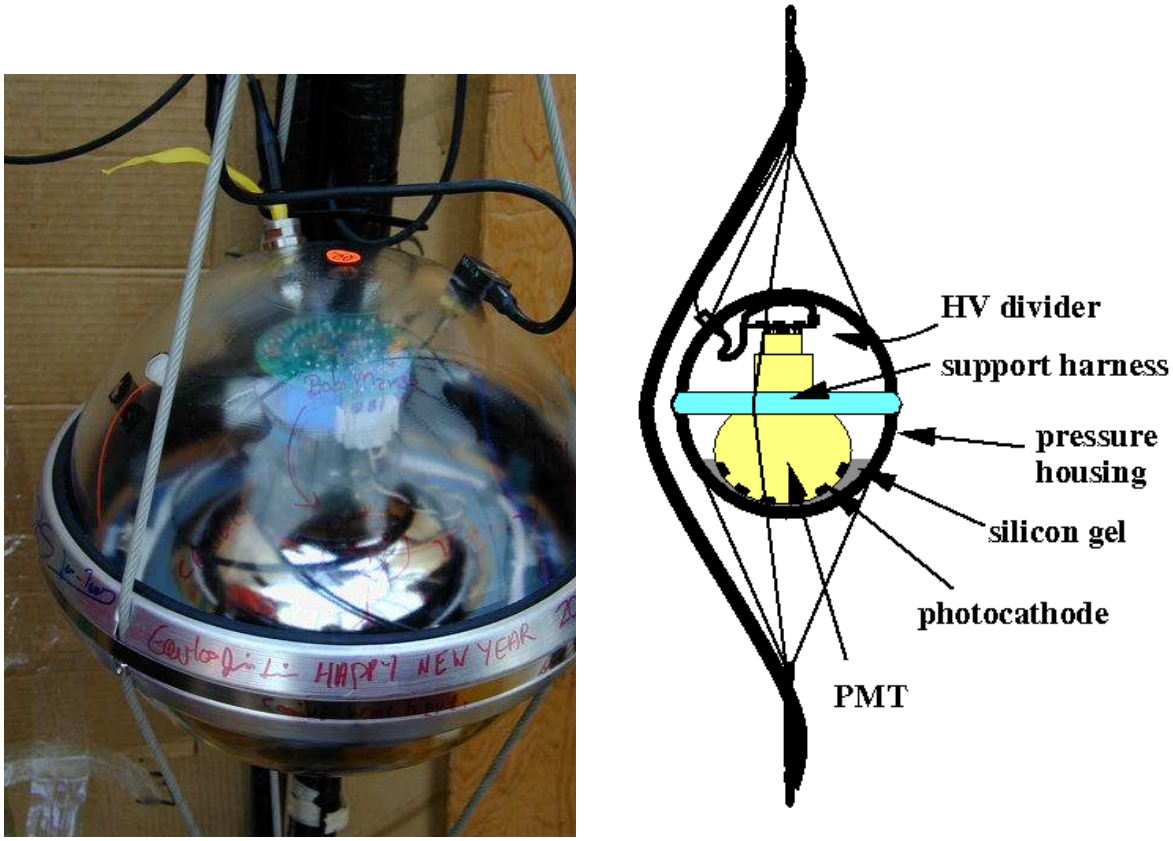

Figure 4.6: Optical module as used in AMANDA [AAB+01]

Fig. 4.6 shows an optical module. Additionally to the PMT, the pressurized vessel also contains the passive electronics necessary to run the PMT and transmit its signal to the surface. In the four strings forming AMANDA-B4, the connection to the surface is established via coaxial cables. They have the advantage of being well-protected against electronic crosstalk, but unfortunately, they are very dispersive and a distortion of the signal takes place on the way to the surface. Another problem of the coaxial cable is the thickness, the number of possible cables in one string is therefore limited.

For these reasons, the next 6 strings were equipped by twisted pair cables. These are almost dispersion free. Unfortunately a great deal of cross-talk takes place.

The next 9 strings have twisted pair and optical fibres. Optical fibres are almost dispersion- and crosstalk-free. But they are fragile, so almost 10% of these fibres broke while being frozen. On string 18, the first digital optical modules (DOM) were deployed. In the DOMs, the module settings are digitally controlled and PMT pulses are internally digitised into waveforms.

4.2.3 Deployment

Deployment takes place during the summer seasons only. The holes are drilled by a pressurised hot water drill to a depth of more than 2 km. After drilling, deployment has to follow immediately as the holes do not stay open, but refreeze. A string has to be deployed within 35-40 hours after drilling.

Figure 4.7: Drilling hole during deployment

For deployment, the cable is slowly released and each module has to be attached to the main cable using breakouts placed at regular distant intervals. Pressure sensors at the top and the bottom of the cable are used to determine the position of the string.

Figure 4.8: OM being deployed

4.3 Data acquisition

The data acquisition is responsible for read out event information and storing it on disk. The AMANDA DAQ is located at the surface in the MAPO-building at the right edge of Fig. 4.3. The event information contains leading and trailing edge time of the last 8 resolved pulses, the largest amplitude of those of them which lie in a 4 μsec window centred at the trigger time and a GPS time stamp. Fig. 4.9 shows a schematic picture of the AMANDA data acquisition.

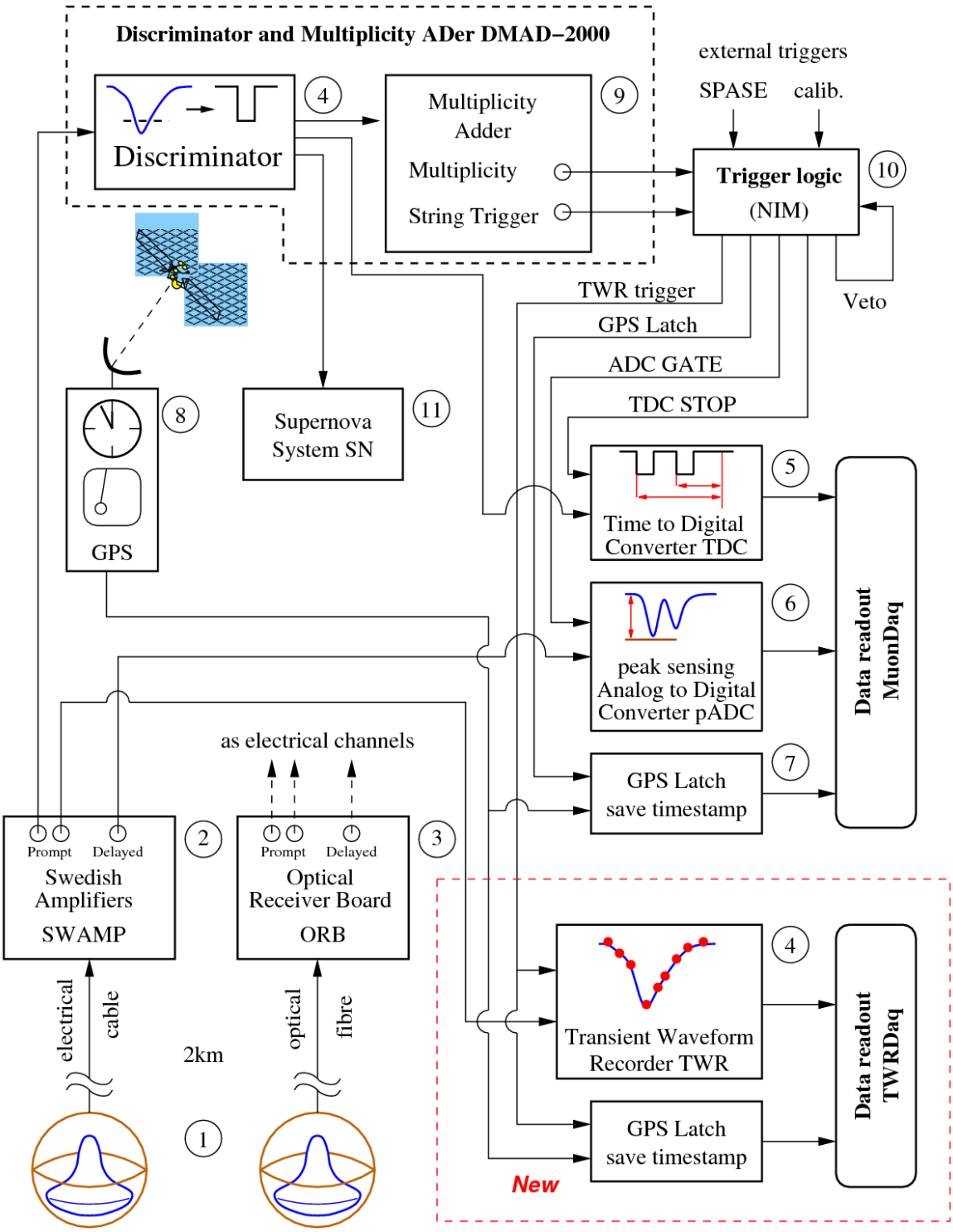

Figure 4.9: Illustration of AMANDAs MuonDAQ [Wag04] In this work, the MuonDaq is used as the TWRDaq was implemented in a later phase

If an OM ① sends a pulse to the surface, the pulse is received by an amplifier ② which

amplifies the signal. There, it is split into a prompt and a delayed signal. The prompt signal goes to the discriminator ④ where it is converted to a logic pulse. The output from the discriminator goes into a digital multiplicity adder (DMADD)⑨. The DMADD sums up the signals from all PMTs within fixed time windows. If the summed up signal reaches a defined threshold, the DMADD sends a trigger signal to subsequent electronic systems. If a trigger signal from the DMADD is received, peak ADCs (analog-to-digital converter which digitize only the maximum voltage value of a pulse)⑥ and fast TDCs (Time to Digital Converter)⑤ read the peak times and heights. The event information is transferred to a computer, which stores it. The MuonDAQ system has a dead time of about 2.2 ms [Tep09].

The trigger used in this work is a multiplicity which demands that at least 24 OMs have recorded at least 1 photo-electron in a time window of 2.1 μsec. With this trigger condition, AMANDA-II reaches a trigger rate of ~ 100 Hz.

Chapter 5

Analysis

5.1 Input data-set - nanoDST

The data which is used in this study is usually rejected as background and consists of the down going muons produced in cosmic ray interactions with the atmosphere of the southern sky. It was collected with the AMANDA-MuonDaq and stored on nano data summary tapes. In the nanoDST, data is stored in ROOT tree structures, a special data storage format of the ROOT data analysis framework. ROOT[1] is an object-oriented analysis framework created to handle and analyse large amount of data. Because the background is very large, only a small part of information is stored. There is information about time, hits, direction, and trigger. What is stored on the nanoDST is described here:

- Time-related information:
  - Modified Julian day
  - Seconds
  - Nanoseconds
  - Run number
- Energy-related information:
  - Number of hits
  - Number of hit channel
  - Number of hit strings
- Direction-related information:
  - Phi (reconstructed)
  - Theta (reconstructed)
- Trigger-related information
  - Multiplicity trigger

[1] `http://root.cern.ch`

- String trigger
- SPASE[2] trigger
- other software trigger

5.1.1 Time-related information

The regular Julian day (JD) is the number of days passed since first of January of the year 4713 before Christ. The Julian day begins at 12 GMT. January, 1st, noontime in Great Britain in 2000 was Julian day number 2 451 545,0. The modified Julian day (MJD) starts November 17, 1858 at Greenwich midnight. The MJD is related to the JD as $mjd = jd - 2400000.5$. AMANDA uses the modified Julian day as continuous time. The MJD has the advantage of changing the date at midnight. Furthermore, it is not that a big number as the JD. Seconds and nanoseconds are always counted from the start of the current day.

5.1.2 Energy-related information

From the number of hits, it is possible to measure the track length, which is related to the energy of the particle. The nanoDSTs contain:

- nHits: This is the sum of all peaks in the PMT signal. nHits can be larger than the number of hit OMs because there can be several peaks per OM which can be separated in time.

- nCh: The number of hit OMs, independent from whether an OM has been hit once or several times. In AMANDA, the OMs are also called "channels".

- nStr: The number of hit strings independent from how many OMs have been hit on the string.

5.1.3 Directional information

Reconstructed values for the detector coordinates are stored as directional information. The reconstruction is done via direct-walk [Ste01]. This is an online, fast track search algorithm without hit cleaning. It is used as a first guess method to determine the direction of charged particles tracks. The Direct-Walk algorithm is also used as hit selection process on an event by event basis.

The Direct-Walk algorithm performs 3 steps: First it searches for so-called "track elements". These are coincidences of two direct hits. Direct hit is when two hits occur with a time difference about equal to the flight time of the muon. The connecting line between the two hit OMs gives a good approximation for the position and direction of the track.

[2]South Pole Air Shower Experiment

In the second step, track candidates are selected from the track elements. According to a typical muon pattern, the track candidate should bring a sufficient number of hits (N_{hit}), a minimum track length (L), a minimum hit density along the track and a good angular accuracy (σ_ψ). The following quality criteria are applied for all hits (i) within

$$-30\,\mathrm{ns} < \delta t < 300\,\mathrm{ns} \qquad \text{and} \qquad \rho < 25\sqrt[4]{\delta t + 30\,\mathrm{ns}}\,:$$

where δt is the time residual and ρ the distance of the OM to the track.

$$\begin{aligned} N_{hit} &> 10 && \text{(Number of hits)} \\ \sigma_L = \frac{1}{N}\sum (L_i - \overline{L})^2 &> 30\,\mathrm{m} && \text{(spread of hits along the track)} \\ \sigma_\psi = \frac{20\,\mathrm{m}}{\sqrt{N_{hit}}\cdot\sigma_L} &< 0.15 && \text{(approximate angular acuracy)} \\ \frac{N_{hit}}{L} &> 0.04 && \text{(hit density along the track).} \end{aligned}$$

If more than one track candidate is found, in the third step the theta angles are sampled into a histogram and a peak is searched. From the bin containing the peak and its adjacent bins, an average zenith angle $< \theta >$ is calculated for the track and the track candidate with the largest hit density is chosen to represent the track. Its θ-value is set to $< \theta >$.

Not or badly re-constructable events are set to $\phi = 0$ or $\theta = 0$. The angular resolution reached with this method is around 5° for atmospheric muons [Ste01].

5.1.4 Trigger information

Every event has also information stored about which trigger condition it fulfilled. Most frequently occur the multiplicity and string trigger. For the multiplicity a certain number of OMs have to register photo-electrons within a small time window (in this case: 24 OMs within 2.1μsec), while the string trigger requests a certain number of OMs on one string. The vast majority of triggers are due to muons from cosmic ray air showers with a mean primary energy of 10 TeV [Chi03]. Furthermore, AMANDA can be triggered from SPASE, an air shower experiment at the surface. There are other triggers which are not explained here as they are not used in this work.

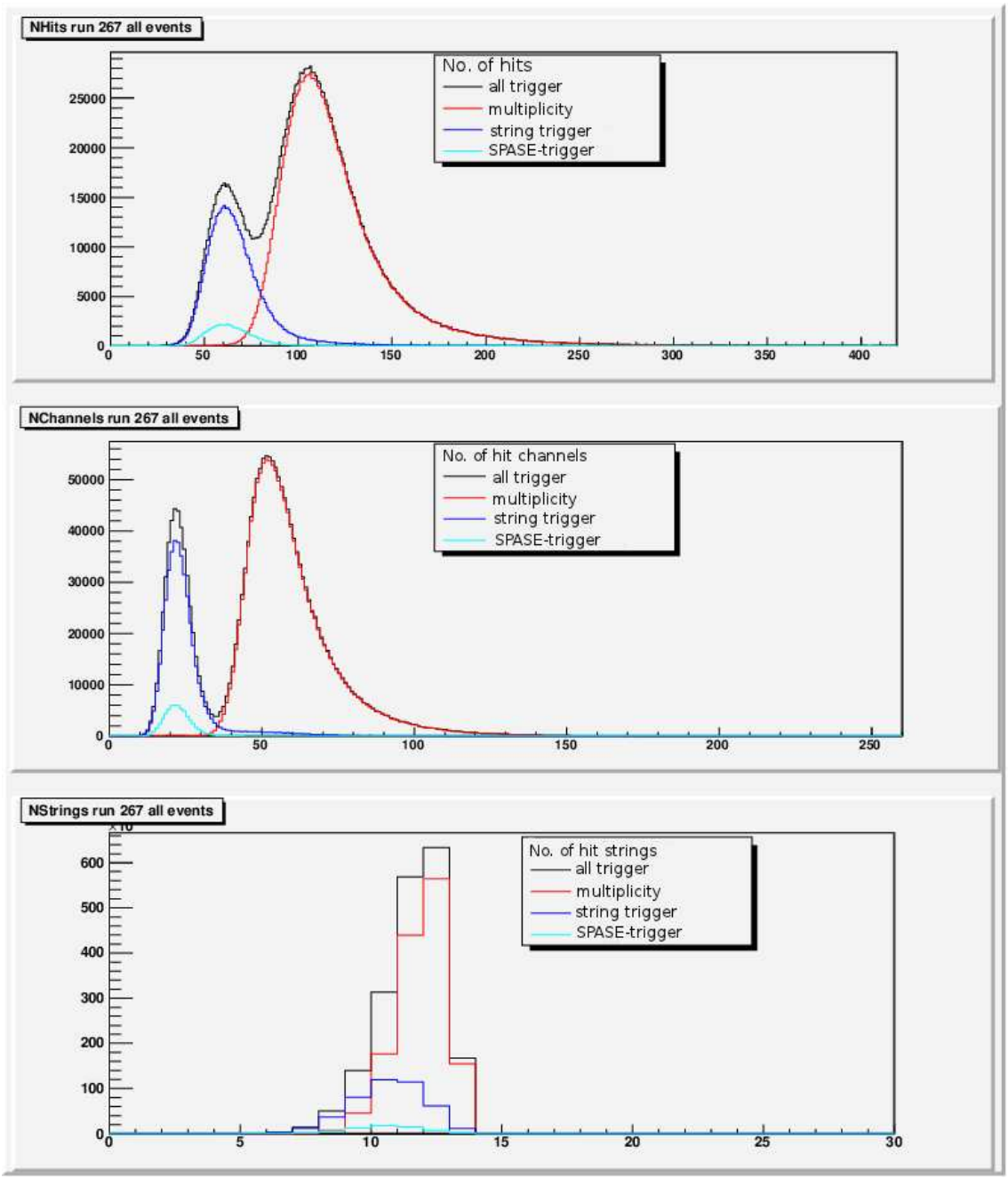

Figure 5.1: Number of hits, number of hit channels and number of hit strings for run 367, 2000, showing the main triggers.

5.1.5 Numbers

The raw dataset consists of $\sim 10^{10}$ events.

Year	Events (10^9)
2000	1.4
2001	2.3
2002	2.4
2003	2.2
2004	2.5
2005	2.6

Table 5.1: Number of events in raw data-set for each year.

5.2 Cuts and filters

In several steps, the input data as described in the last section, is processed. This is necessary, because it is of crucial importance in an anisotropy study to find, take account for, and correct possible systematic errors within the detector.

Run selection

The AMANDA monitoring page[3] gives an overview of "good" and "bad" runs. All runs marked as "Short run" or "Special run" (calibration or detector test runs) were rejected.

Time

From the selected runs, in the very first step, the TTree within the nanoDST, as described in the section before, is read out and a timing filter is applied to filter out events with bad time stamps (mainly timestamps not in chronological order).

Trigger

As can be seen in Fig.5.1, the data are composed of several triggers. Fig.5.1 shows the nHits, nCh, and nStr distributions from a single, randomly chosen run. It is clearly visible that the multiplicity trigger is well suited for this analysis. All events which fulfilled the trigger conditions of the multiplicity trigger were chosen, independently from whether they fulfilled also other conditions or not.

Theta and phi

A very important cut is on ϕ and θ. The first guess method, used in reconstruction, set the angles of bad reconstructable or misreconstructed events to 0°. Therefore, it is necessary to cut on ϕ and θ. Fig.5.2 and Fig.5.3 show the distributions of ϕ and θ without multiplicity trigger cut, respectively. Top panels show the distributions without the cut. It is clearly visible that there must be a cut on 0, even though lots of data get lost. The cuts were set to $\phi > 0.1°$ and $\theta > 0.2°$

[3] `http://thorin.physik.uni-mainz.de/amanda-monitoring/html/`

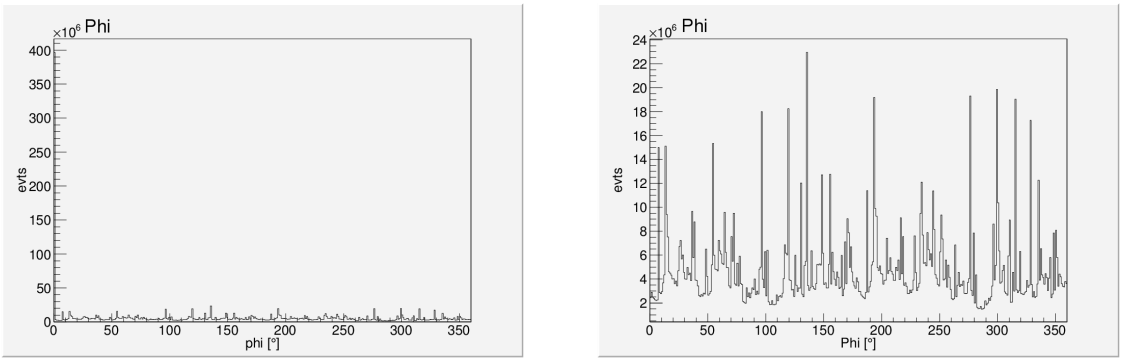

Figure 5.2: Phi distribution, left without any cut, right with cut on 0° (The multiple-peak structure results from the clustering of events in direction of the strings).

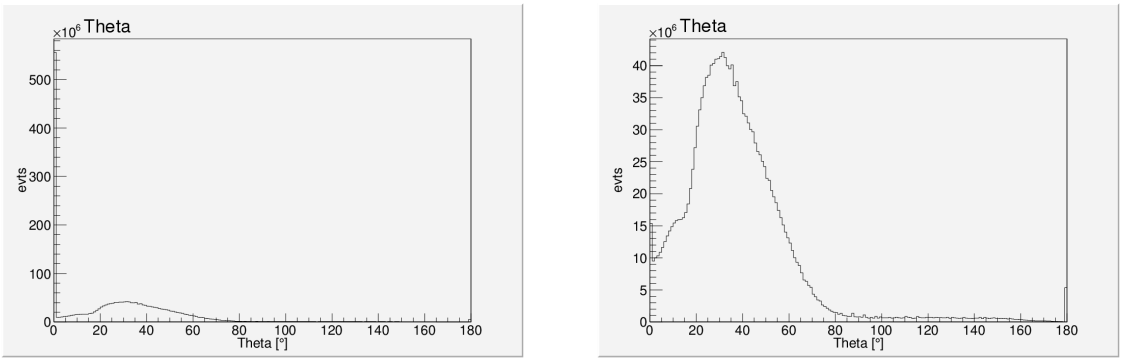

Figure 5.3: Theta distribution, left without any cut, right with cut on 0°

5.3 Stability considerations

5.3.1 Data selection

To search for cosmic ray anisotropies, a detector must be sufficiently stable. It is therefore very important to analyse its stability. Analysed are the counting rates and the distribution of the local azimuth for each single year. In a preparative step, the data is scanned in 5 minute bins. Bins with data gaps longer than 1 second are rejected. Fig. 5.4 shows the effect of this procedure on the counting rate for year 2000.

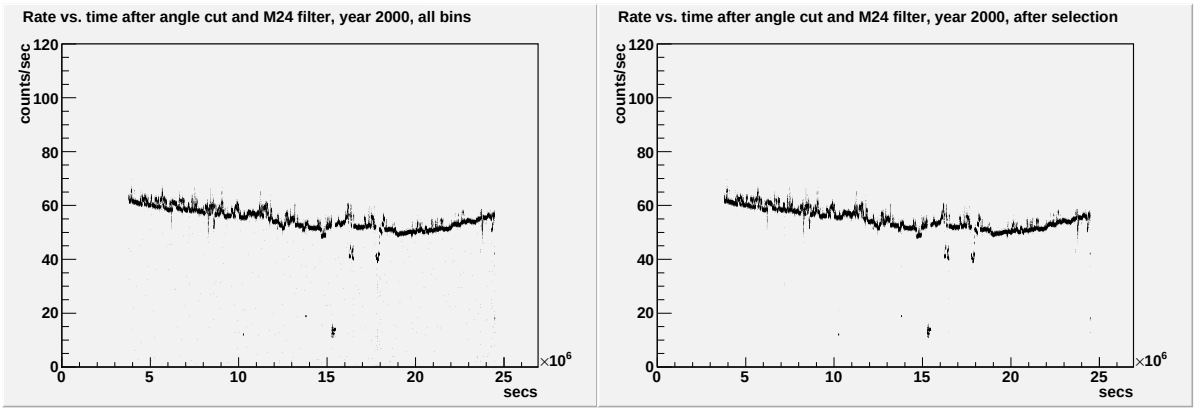

Figure 5.4: Counting rate for year 2000 with (left side) and without (right side) bins containing gaps > 1 sec

The year 2004 and the VLF-beacon

Due to a very low frequency signal from a VLF-beacon used for another scientific experiment at the South Pole, AMANDA data acquisition needed to be turned off for 1 minute every 15 minutes during 2004. The data selection used for the other years described above would have led to a loss of data between 30% and 60%, which made it necessary to treat the data from 2004 differently. Therefore, the data from 2004 was not scanned in 5 minute bins, but 14 minutes with a break of one minute after each bin. As the sending times of the VLF-beacon are known exactly, it was still possible to use 2004 data. The further processing of these data is identically to the other years.

5.3.2 Counting rates

The normal rate after the cuts and filters is about 60 Hz. For the stability considerations, a procedure is adopted where 5-minute rates of each hour are compared to the average of the previous 12 hours.

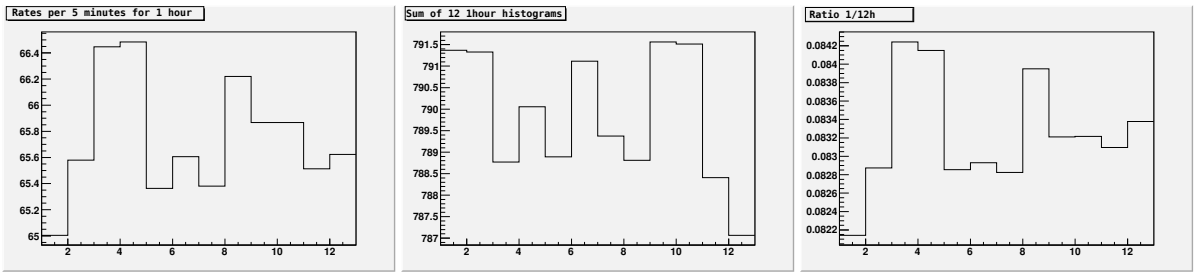

Figure 5.5: Illustration of steps 2 to 4 (see text).

- **First step:** Calculation of rates per 5 minutes: From each of the 5 minutes bins a rate is calculated

- **Second step (Fig. 5.5 leftmost):** The rates calculated in first step are filled into a histogram containing 12 5-minute rates (Figure: Example of an one-hour-histogram).

- **Third step (Fig. 5.5 middle):** 12 of these histograms from second step are summed up (Figure: Example of a histogram containing the sum of 12 histograms from first step).

- **Fourth step (Fig. 5.5 rightmost):** Starting from no. 13, each single one-hour histogram is divided by the sum of the 12 preceding one-hour histograms (Figure: Example of a histogram resulting from the division of a one-hour-histogram from first step and the sum from second step).

- **Fifth step:** From the histograms resulting from the division, the deviation of the mean value from a fix mean 1/12 is calculated:

$$MeanDev = (Mean - FixMean)/FixMean$$

  and plotted into a histogram (Fig. 5.6).

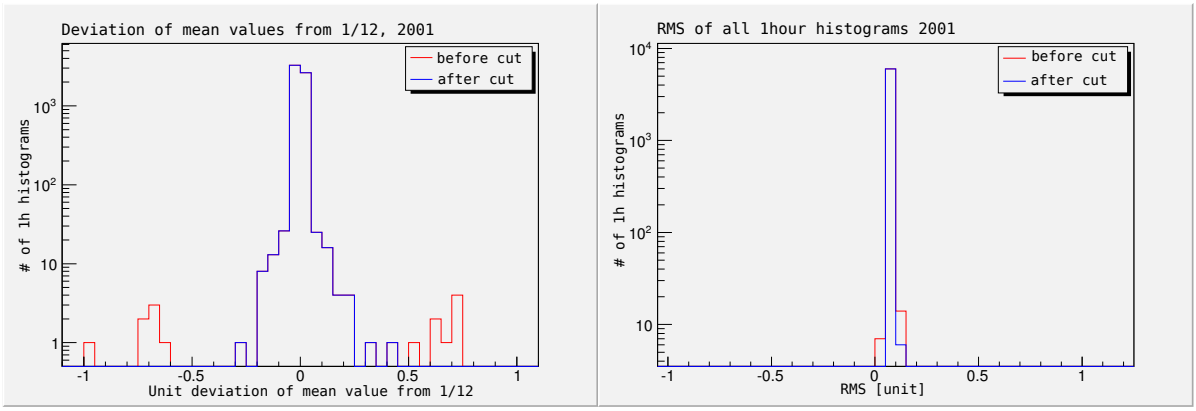

Figure 5.6: Deviation of mean values from 1/12 and rms 2001

Fig. 5.6 shows that the counting rate of the detector is quite stable. To rule out times with strong fluctuations, intervals where the mean value deviates more than 50% are rejected.

5.3.3 Local azimuth distribution

For the stability of the local azimuth, a method analogous to the one presented in the previous section was applied:

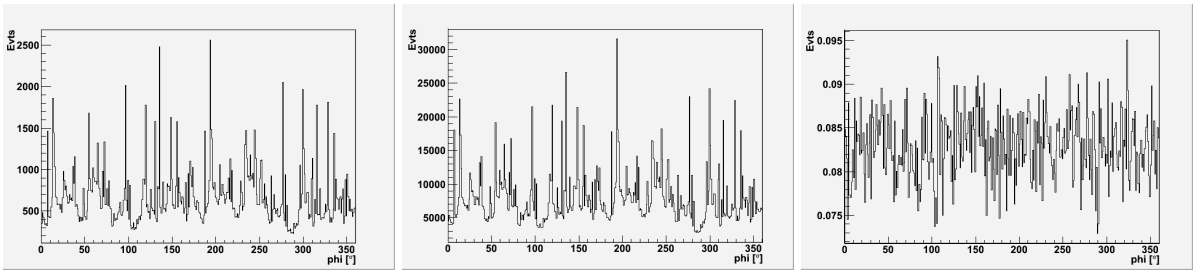

Figure 5.7: Illustration of steps 2 to 4 (see text).

- **First step:** A histogram with the detector phi distribution is filled for each 5 minutes bin
- **Second step (Fig.5.7 leftmost):** The phi distributions of 12 consecutively filled 5 minute bins are plotted in an one-hour histogram (Figure: Example of an one-hour-histogram).
- **Third step (Fig.5.7 middle):** 12 of these histograms from second step are summed up (Figure: Example of a histogram containing the sum of 12 histograms from first step).
- **Fourth step (Fig.5.7 rightmost):** Starting from no. 13, each single one-hour histogram is divided by the sum of the 12 preceding one-hour histograms (Figure: Example of a histogram resulting from the division of an one-hour-histogram from the first step and the sum from second step).
- **Fifth step:** From the histograms resulting from the division, the deviation of the mean value from a fix mean 1/12 is calculated:

$$MeanDev = (Mean - FixMean)/FixMean$$

and plotted into a histogram (Fig.5.8).

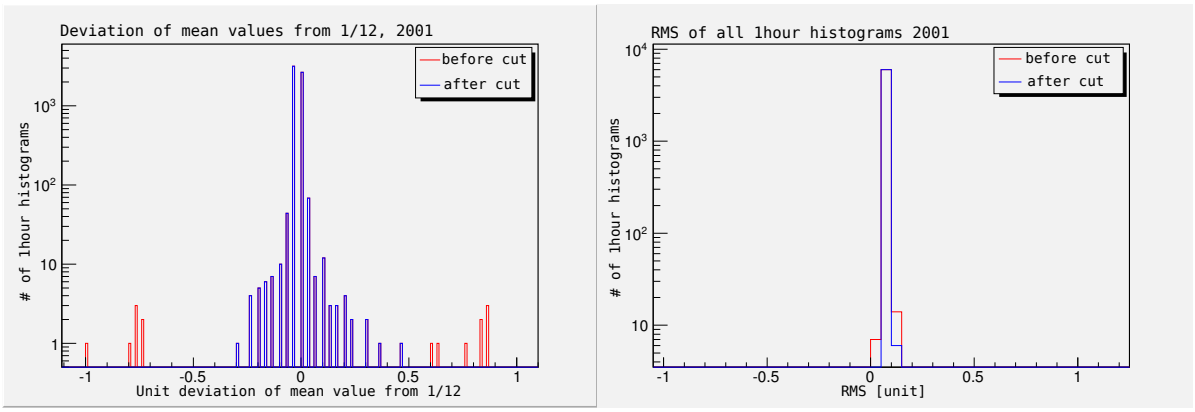

Figure 5.8: Deviation of mean values from 1/12 and rms 2001

Fig.5.8 shows that also the local azimuth distribution is sufficiently stable. Intervals where the mean value deviates more than 50% are discarded.

5.4 The final data-set

The complete final data-set consists of a total of $7.98 \cdot 10^9$ events. For each single year this is:

Year	Events (10^9)
2000	1.04
2001	1.34
2002	1.02
2003	1.53
2004	1.31
2005	1.65

Table 5.2: Number of events in final data-set for each year.

Only runs marked as "Long run" on the AMANDA monitoring website were used, events where a proper directional reconstruction could not be performed were rejected. Only events fulfilling conditions of multiplicity trigger were used. Events recorded during phases where the detector did not seem stable were rejected. All these measures lead to a loss of $\sim 50\%$ of data. Anisotropy studies need high statistics, but also clean and stable data. As the trigger rate of the AMANDA experiment is sufficiently high, it is possible to reach both, high statistics as well as stable data.

5.5 Corrections

5.5.1 Right Ascension

The Right Ascension needs to be corrected for non-uniformities within the sky coverage. These non-uniformities are principally due to the non-uniformity of the detector itself as well as due to maintenance, calibration or other experiments leading to instabilities in data taking.

The basic idea of the RA-correction is to use the 5 Min intervals without gaps as exposure units. In the technical realisation the orientations in right ascension of the exposure units were monitored. For each valid 5 Min bin the Right Ascension was calculated for $\varphi = 0$, $\theta = 0$ and the value for corresponding Right Ascension bin in a histogram increased by 1. From the resulting histogram the correction factor is calculated as the inverse value for each bin. This has been done for each annual data set.

The histogram resulting from this procedure is shown in Fig.5.9. Basically, it shows how long each 3°-Right Ascension bin was observed by the detector during year 2001.

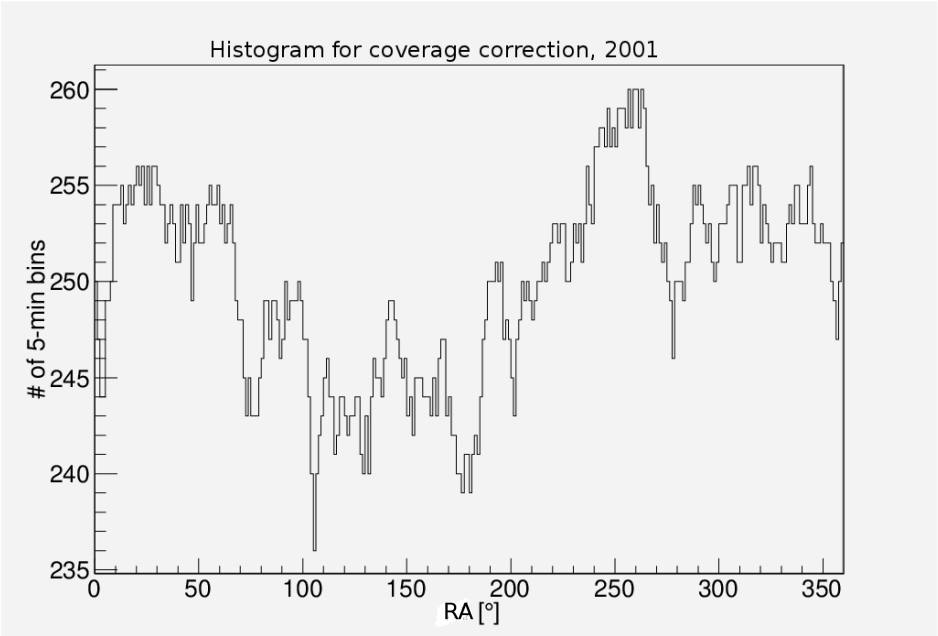

Figure 5.9: Sky coverage histogram for RA-correction, year 2001

5.5.2 Phi

The geometrical structure of the detector consisting of several strings with optical modules leads to a clustering of events towards the directions of the strings showing up as strong peaks in the detector phi distribution.

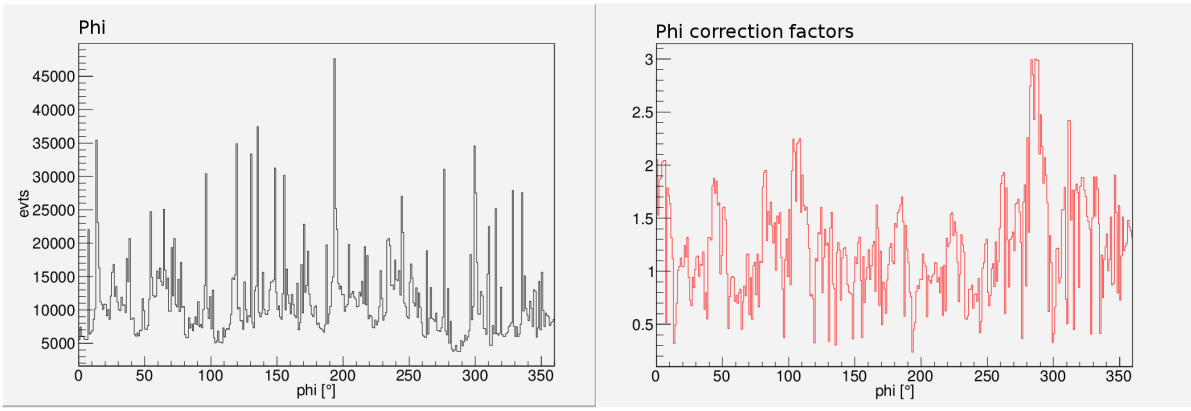

Figure 5.10: Example of a detector phi distribution for one day (left panel) and of the correction histogram for the same day (right panel)(day 51697, 2000)

This distribution has to be flattened by giving a proper weight to every phi angle.

The weight is calculated by the mean of each histogram as

$$weight = \frac{mean}{phi}.$$

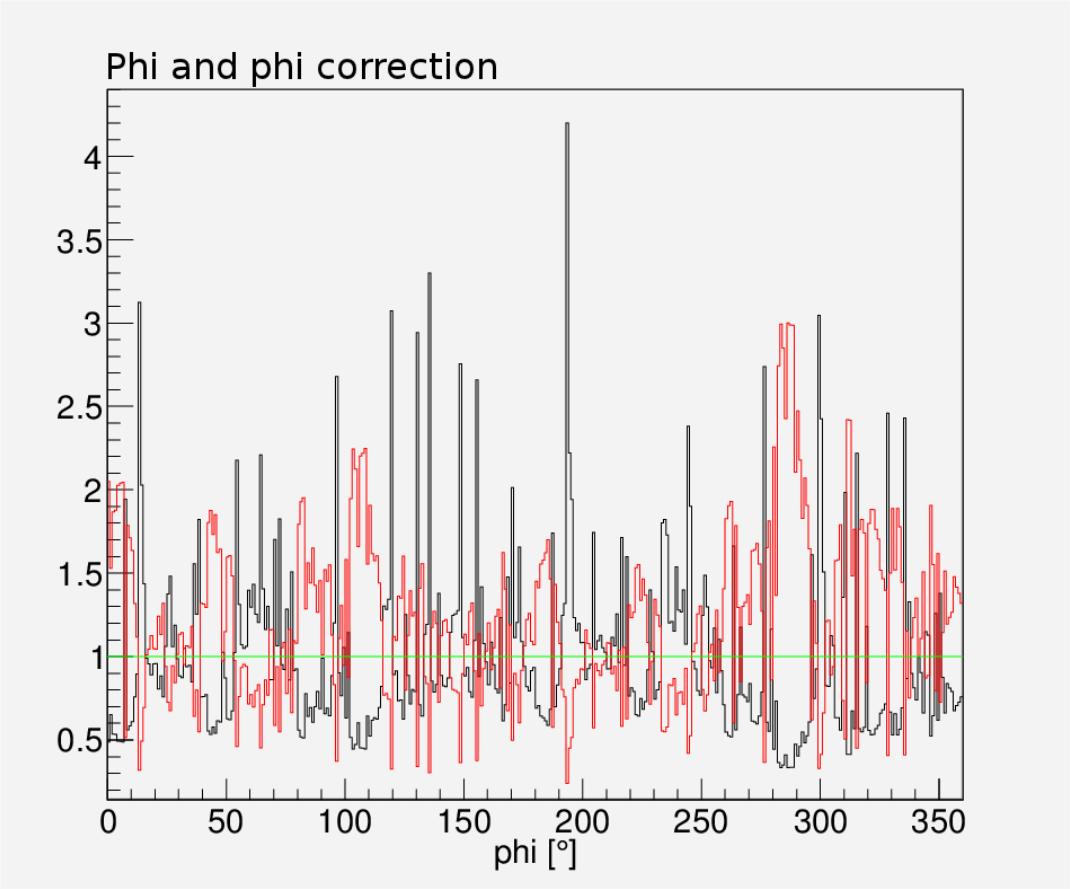

Figure 5.11: The phi correction. Black line: normalised phi distribution (normalisation only for demonstration), red line: correction factors, green line: the product of the other two

How long the time unit for the correction histograms may be is limited to short times by the statistics and to long time intervals by the stability of the detector. In this work, daily correction histograms have been used as the detector and its event reconstruction is stable enough during this time interval.

Fig.5.12 shows the effect of the corrections.

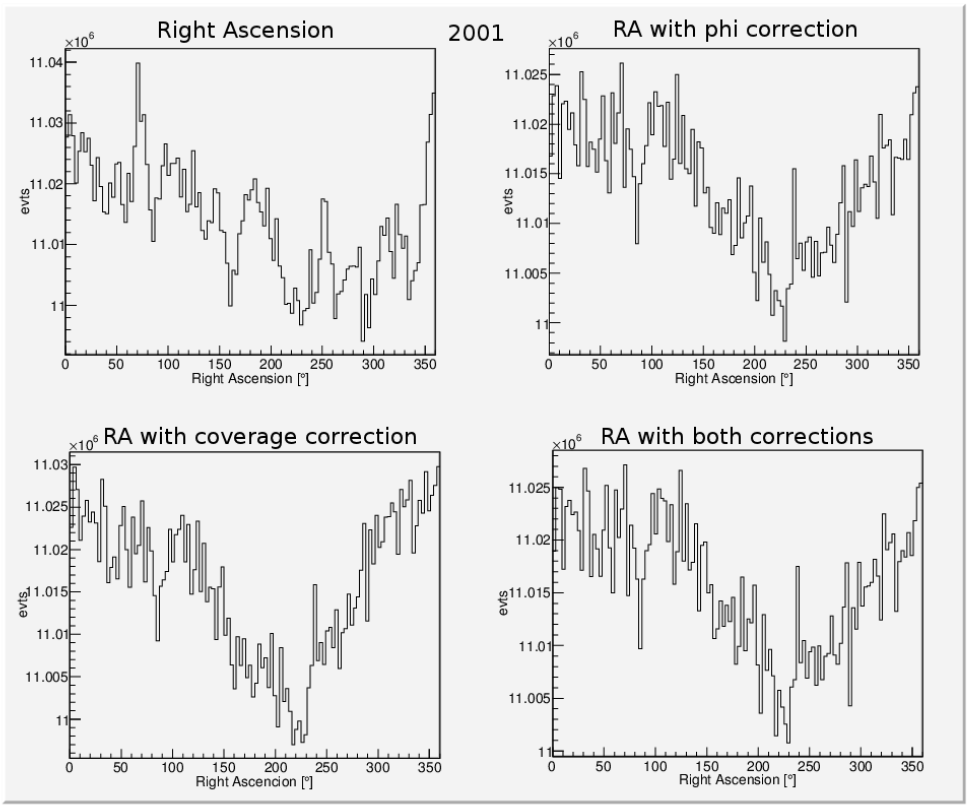

Figure 5.12: Right ascension distributions with and without corrections. Top left: without correction, top right: with phi correction, bottom left: with RA correction, bottom right: with both corrections (year 2001)

Chapter 6

Results

6.1 Analysis of the full data period (2000-2005)

After the cuts and corrections discussed in the previous chapter have been applied, all the data have been taken together, accounting for the corrections for each individual year. The data were collected between 2000-2005, leading to a total amount of $7.8 \cdot 10^9$ events after the cuts.

6.1.1 1-dimensional analysis

First order harmonic fit

For the analysis, the RA-distribution of the full data period (2000 to 2005) was fitted with the function

$$I(x) = N \cdot \sin(x + \varphi) + y, \tag{6.1}$$

where N is the amplitude and φ the phase of the anisotropy in radian. The parameter y denotes the offset from 0. The results are shown in Fig.6.1.

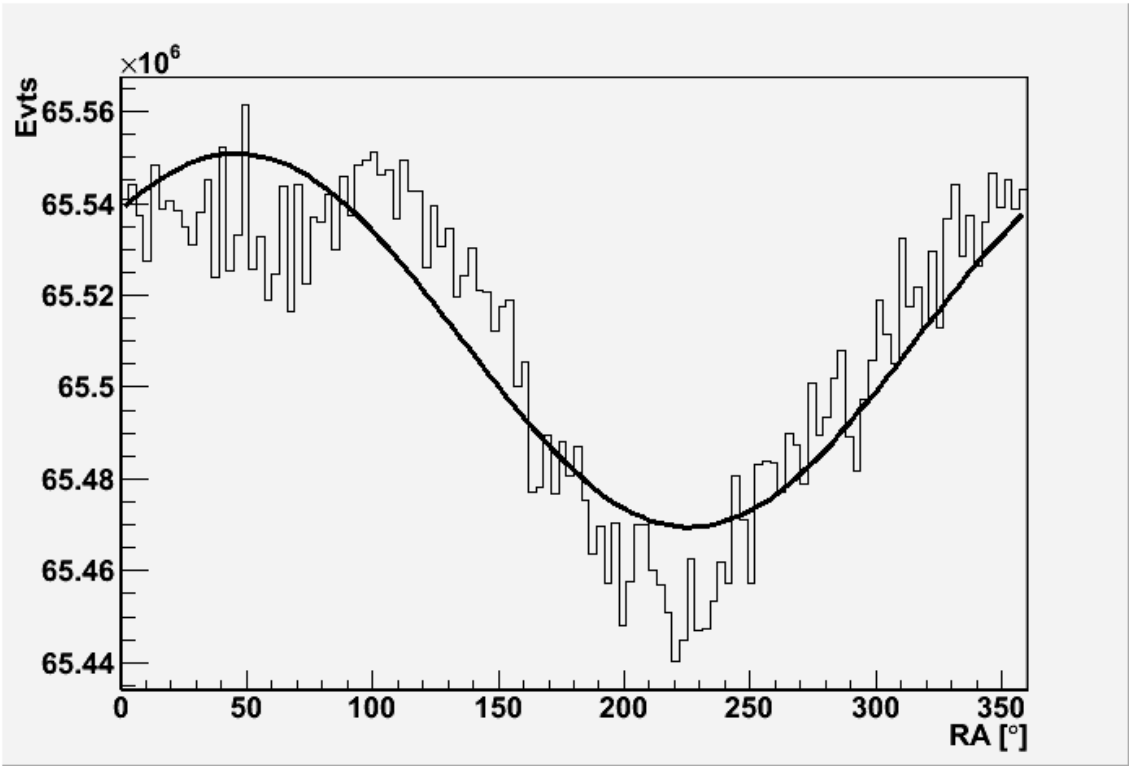

Figure 6.1: RA distribution 2000-2005 with first order harmonic fit

Fig.6.1 shows the variation of the counting rates in right ascension for the full data period after application of the corrections discussed in the previous chapter, and the fit function described above.

Second order harmonic fit

In order to find out whether the anisotropy seen is of a pure dipole structure, the data were also fitted to a two order harmonic function:

$$I(x) = N_1 \cdot \sin(x + \varphi_1) + N_2 \cdot \sin(2(x + \varphi_2)) + y. \tag{6.2}$$

The result is shown in Fig.6.2.

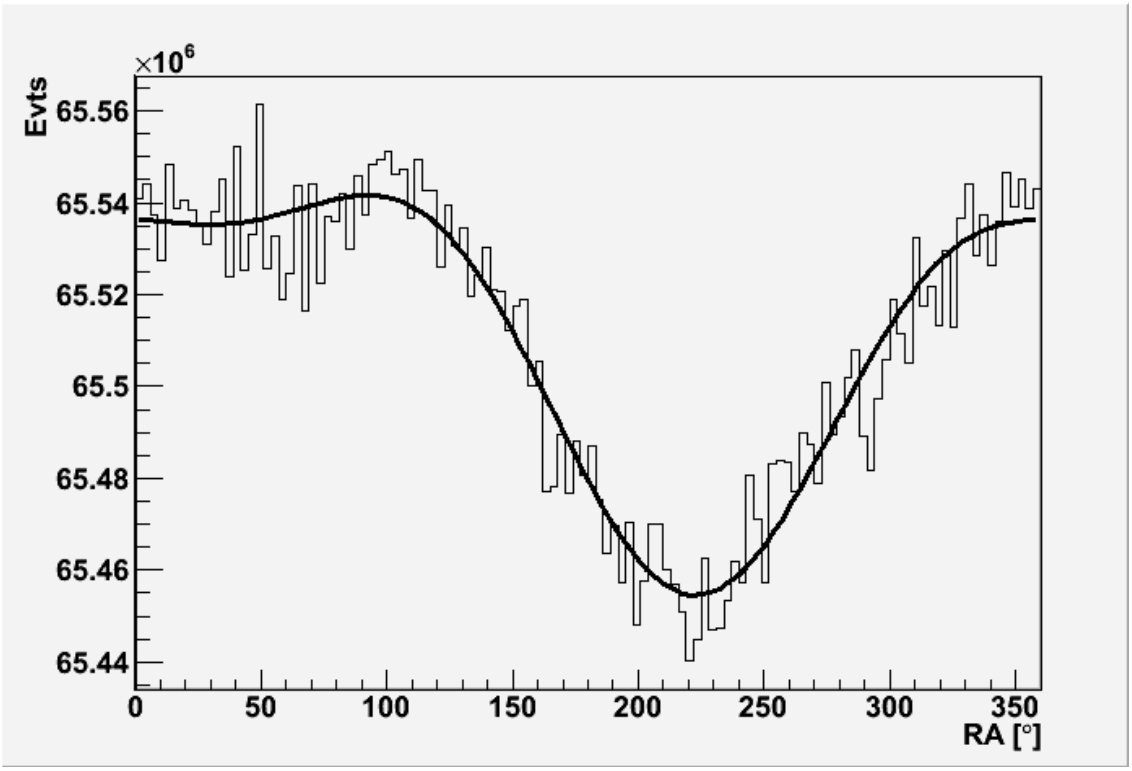

Figure 6.2: RA distribution 2000-2005 with second order harmonic fit

First and second order relative amplitude and phase as well as χ^2/ndf of the fit functions are summarised in Tab. 6.1. The relative amplitudes A_1 and A_2 are calculated from N_1 and N_2 in Eq. (6.2) by dividing them by the offset y. The phases ϕ_1 and ϕ_2 are the first and second order phase from Eq. (6.2) in degree.

	χ^2/ndf	$A_1(10^{-4})$	$\phi_1[^\circ]$	$A_2(10^{-4})$	$\phi_2[^\circ]$
1st order	365/117	6.20 ± 0.16	44.2 ± 1.5	-	-
2nd order	158/115	6.20 ± 0.16	44.2 ± 1.5	2.93 ± 0.16	274.3 ± 2.4

Table 6.1: Fit parameters, amplitudes and phases from first and second order harmonic fit for 2000-2005

The analysis shows that the second harmonic does not vanish, which is an indication for that the anisotropy is not a pure dipole.

6.1.2 2-dimensional analysis

The combined data of 2000-2005 provide sufficient statistics also for a two-dimensional analysis. This was done using the software package "HEALPix"[1] [GHB+05]. HEALPix is

[1] see: http://healpix.jpl.nasa.gov

the acronym for Hierarchical Equal Area isoLatitude Pixelization of a sphere. It divides the surface of a sphere into a number of pixels which cover the same area each. The 2-dimensional analysis was performed by producing a reference map to be subtracted from the data. The reference map shows the sky seen by the detector if no anisotropy was present in the cosmic radiation. For its realisation, for every real event, 20 "fake" events were produced by keeping the local angles of the real event but using the times of 20 randomly chosen events within a time of 12 hours before and 12 hours after the real event. For every of these fake events, the right ascension and the declination were calculated and then filled into a sky map with a weight factor of 1/20. The idea behind this map construction is to obtain the same exposure as the real data. A correction for the sky coverage as done for the 1-dimensional analysis is therefore not needed. The reference map is then subtracted from the map created with the real data. This method was adopted from [Abb10].

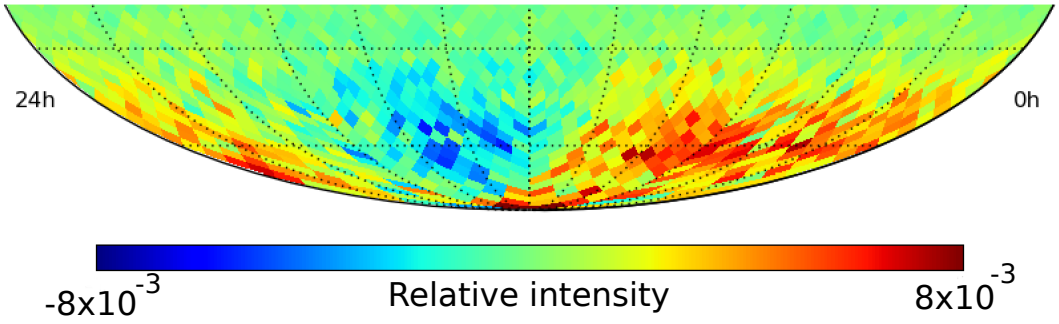

Figure 6.3: Skymap of the anisotropy of the southern sky produced with HEALPix.

Fig. 6.3 shows the sky map produced by HEALPix. The part above $-30°$ has been cut away as the statistics is getting low towards the equator. The map shows the intensity variation left after subtraction of the reference map.

6.2 The single years

6.2.1 First order harmonic fit

In another analysis, each year is examined separately. Therefore, the RA-distributions of every single year from 2000 to 2005 were fitted with the function Eq. (6.1)

The results are shown in Fig. 6.4.

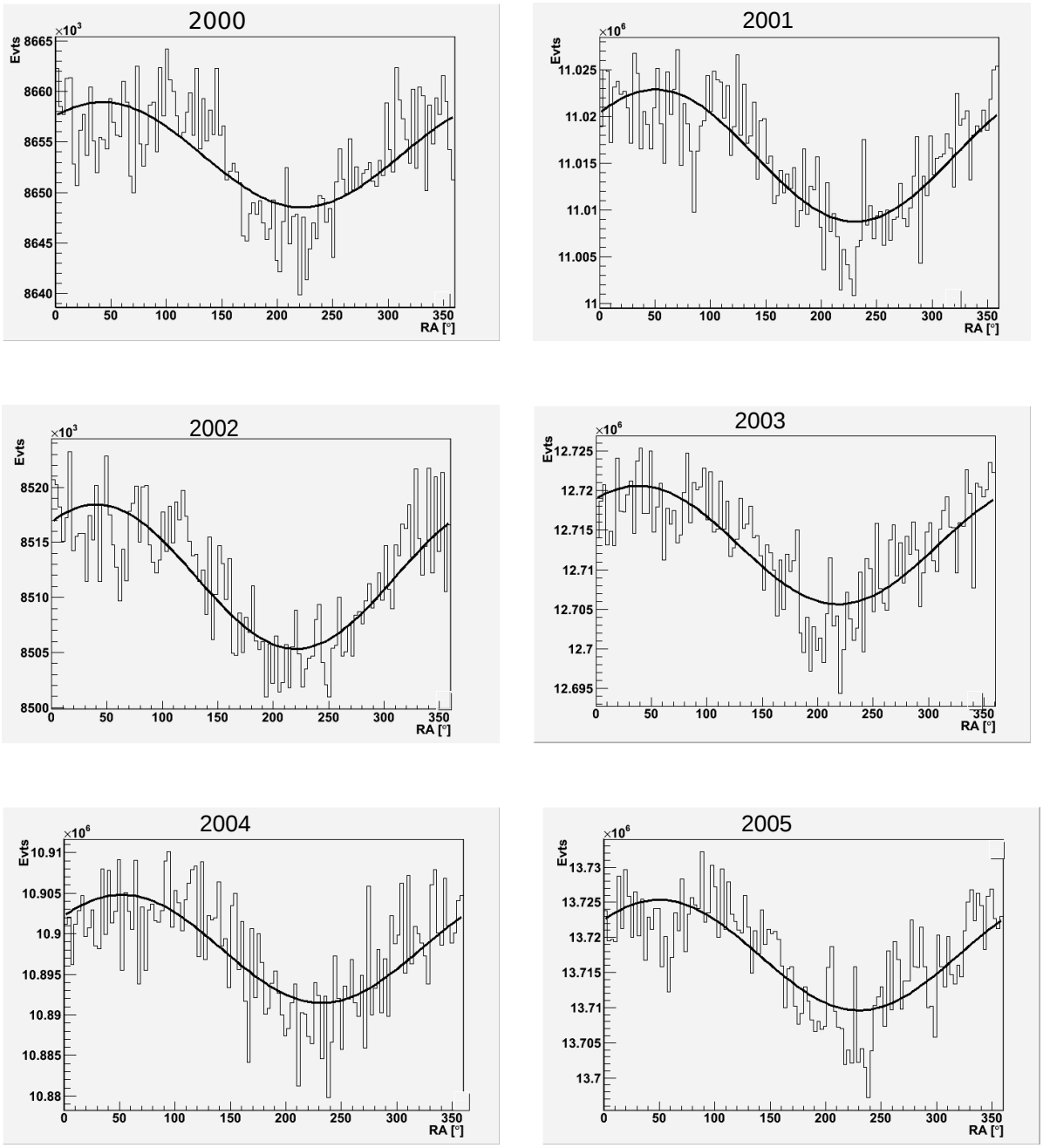

Figure 6.4: First order harmonic fit for the years 2000-2005

The figures in Fig. 6.4 show the variations of the counting rates in right ascension for each single year after application of the corrections discussed in chapter 5, and the first order harmonic fit. Tab. 6.2 shows the relative amplitudes A calculated from Eq. (6.1) as:

$$A = \frac{N}{y}$$

and ϕ the phase φ in degree.

Year	$A_1(10^{-4})$	$\phi_1[^\circ]$
2000	6.02 ± 0.44	47.8 ± 4.2
2001	6.42 ± 0.38	39.6 ± 3.5
2002	7.70 ± 0.44	49.7 ± 3.3
2003	5.87 ± 0.36	51.2 ± 3.5
2004	6.11 ± 0.39	37.8 ± 3.7
2005	5.73 ± 0.35	40.1 ± 3.5

Table 6.2: Amplitudes and phases from first order harmonic fit

All years show a clear anisotropy with a dipole structure. The amplitudes are around $\sim 6 \cdot 10^{-4}$, the phases around 40°. The errors in Tab.6.2 correspond to the statistical error from the fit.

Tab.6.3 shows the quality of the fit function for each single year.

	2000	2001	2002	2003	2004	2005
χ^2/ndf	207/117	154.2/117	148.5/117	173.9/117	249.9/117	204.4/117

Table 6.3: χ^2/ndf for first order harmonic fit

6.2.2 Second order harmonic fit

Additionally, the single years were fitted with the second order harmonic function Eq. (6.2). These fits are shown in Fig.6.5 and Tab.6.4.

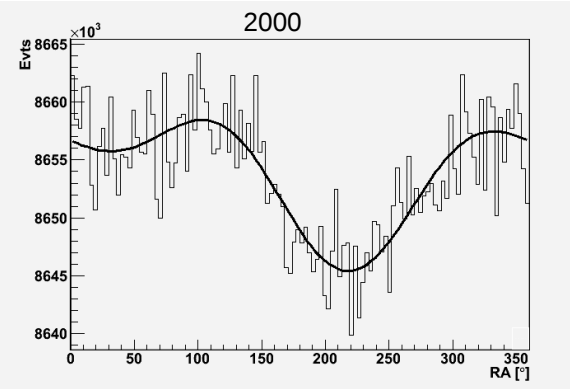

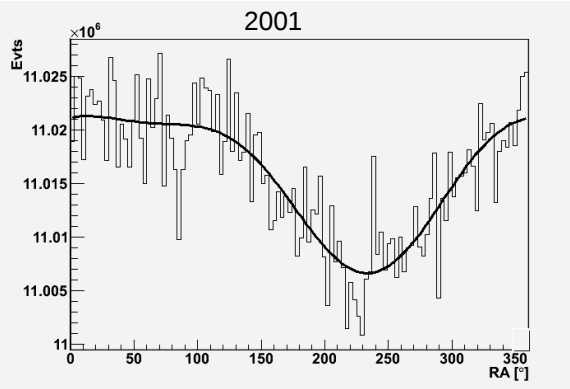

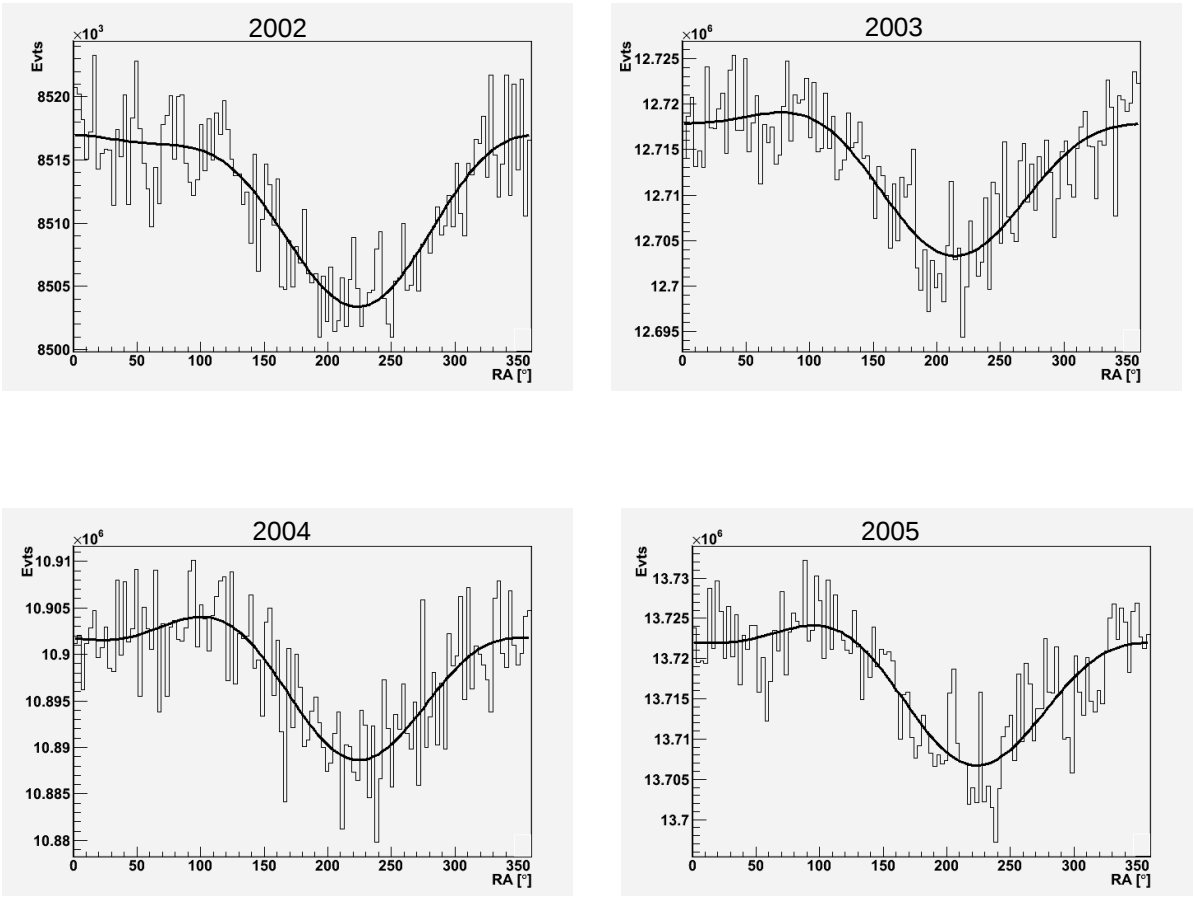

Figure 6.5: Second order harmonic fit for the years 2000-2005

The amplitudes A_1 and A_2 in Tab.6.4 are calculated from Eq.(6.2) as:

$$A_1 = \frac{N_1}{y} \qquad \text{and} \qquad A_2 = \frac{N_2}{y}$$

The phases ϕ_1 and ϕ_2 correspond to φ_1 and φ_2 in degree, respectively.

Year	$A_1(10^{-4})$	$\phi_1[^\circ]$	$A_2(10^{-4})$	$\phi_2[^\circ]$
2000	6.02 ± 0.44	47.8 ± 4.2	3.63 ± 0.44	278.8 ± 3.5
2001	6.42 ± 0.38	39.6 ± 3.5	1.95 ± 0.39	259.0 ± 5.7
2002	7.70 ± 0.44	49.7 ± 3.3	2.30 ± 0.44	88.8 ± 5.5
2003	5.87 ± 0.36	51.2 ± 3.5	1.87 ± 0.36	104.1 ± 5.5
2004	6.11 ± 0.39	37.8 ± 3.7	2.68 ± 0.39	271.8 ± 4.2
2005	5.73 ± 0.35	40.1 ± 3.5	2.18 ± 0.35	275.6 ± 4.6

Table 6.4: Amplitudes and phases from second order harmonic fit

	2000	2001	2002	2003	2004	2005
χ^2/ndf	139/115	129/115	122/115	147/115	203/115	207/115

Table 6.5: χ^2/ndf for second order harmonic fit

6.3 Temporal variation of the anisotropy

The data for the analysis was taken between 2000 and 2005 which is the half of solar cycle 23. The data starts at the maximum of the cycle and goes until close to the minimum. The solar activity does not have a direct influence on the anisotropy analysed here as the sensitivity of the experiment starts above the energy region which is directly influenced by the sun. Nevertheless it is interesting to see whether there are changes in the amplitude or phases indicating a temporal variation within this time period.

Therefore both, amplitudes and phases were fitted for two hypotheses:

1. The observed amplitudes and phases do not vary with time within 6 years:

$$\bar{A_1} = const \tag{6.3}$$

$$\bar{\phi_1} = const \tag{6.4}$$

(solid line in Fig.6.6 and Fig.6.7)

2. The observed amplitudes and phases do vary with time within 6 years:

$$A_1(x) = b \cdot (x - 2002.5) + A_{1,0} \tag{6.5}$$

$$\phi_1(x) = b \cdot (x - 2002.5) + \phi_{1,0} \tag{6.6}$$

(dashed line in Fig.6.6 and Fig.6.7)

A higher order function was not used for fitting the data as it is not expected to see more than a trend within 6 years which is still a very short time on cosmological scale. In Fig.6.6 and Fig.6.7, the values of the amplitudes and phases from the first order fit of each single year are shown with their respective errors and fitted for two hypotheses.

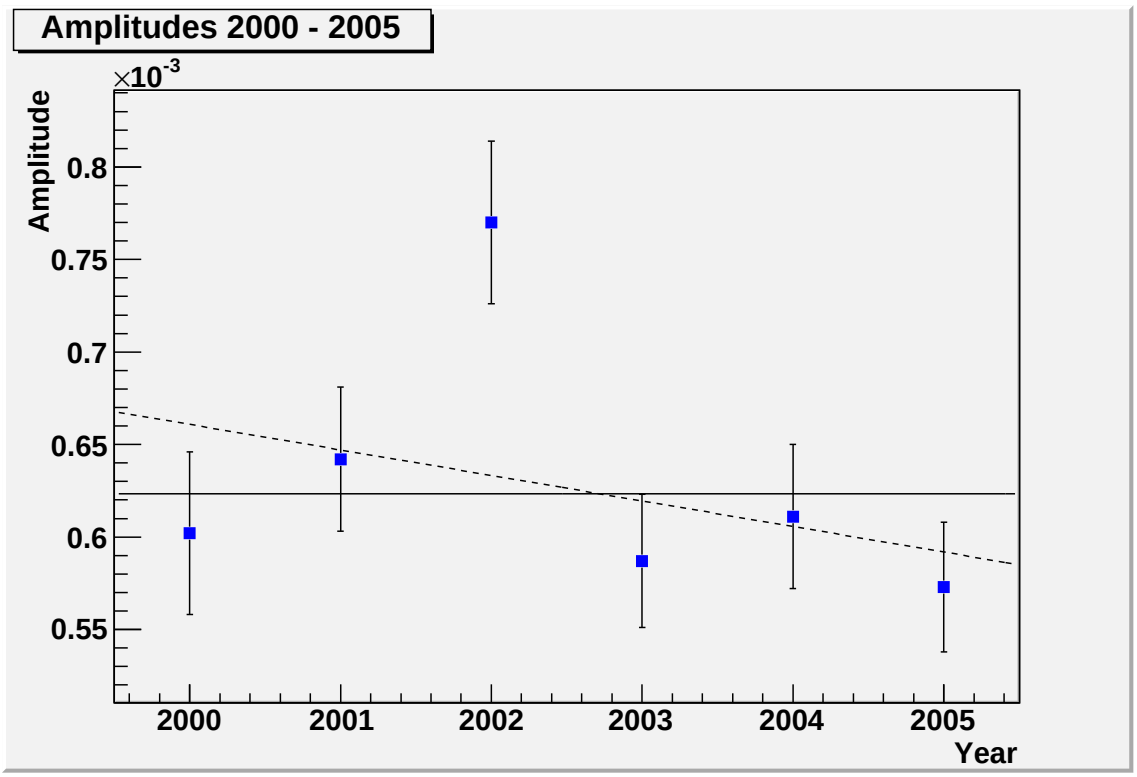

Figure 6.6: The anisotropy amplitudes from 2000 to 2005

Fig. 6.6 shows the amplitudes of the dipole anisotropy for the years 2000-2005. The solid line corresponds to the best fit for a constant function with $\chi^2/ndf = 14.76/5$:

$$\bar{A}_1 = (6.233 \pm 0.159) \cdot 10^{-4}.$$

The dashed line corresponds to best result of the the linear fit with $\chi^2/ndf = 12.59/4$:

$$A_1 = (-1.381 \pm 0.936) \cdot 10^{-5}\mathrm{yr}^{-1} \cdot x + (6.264 \pm 0.161) \cdot 10^{-4}.$$

With $\chi^2/ndf = 14.76/5$ for the constant and $\chi^2/ndf = 12.59/4$ for the linear fit, both functions do not fit the data very well, still the quality of the constant fit is slightly higher.

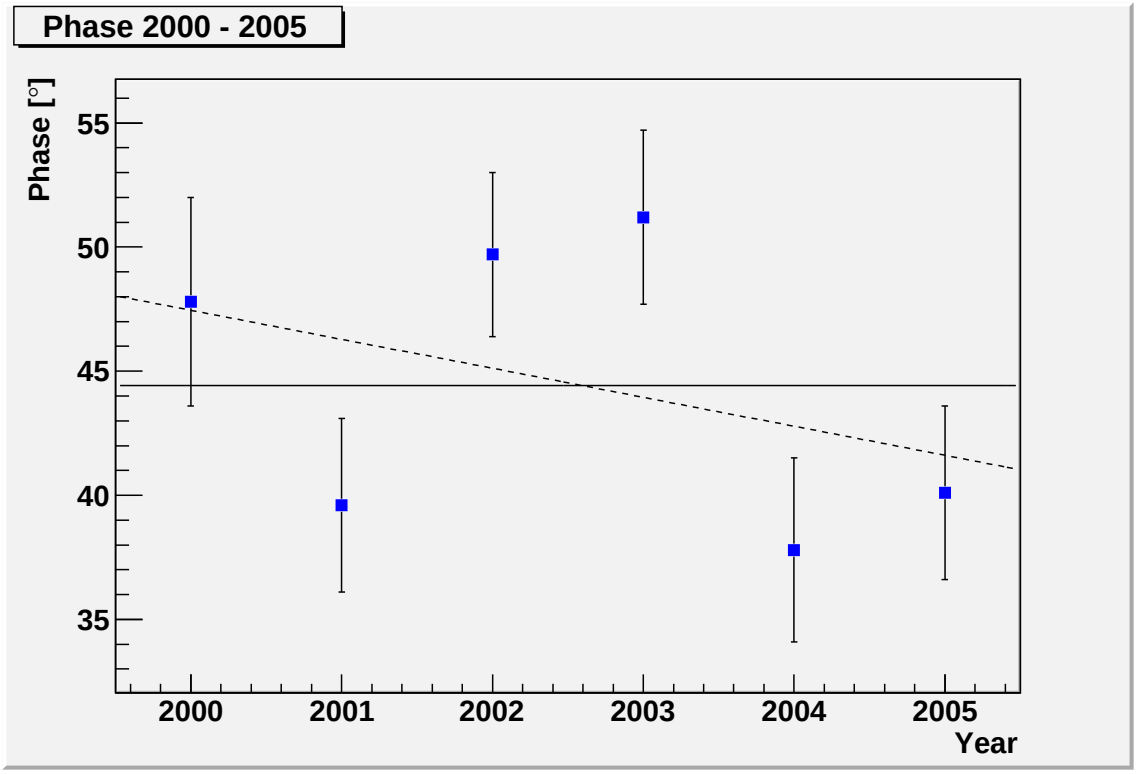

Figure 6.7: The anisotropy phases from 2000 to 2005

Fig.6.7 shows the phases of the dipole anisotropy for the years 2000-2005. The solid line corresponds to the best fit for a constant function with $\chi^2/ndf = 13.58/5$

$$\bar{\phi_1} = (44.421 \pm 1.464)^\circ.$$

The dashed line corresponds to the best result of linear fit with $\chi^2/ndf = 11.78/4$

$$\phi_1(x) = (-1.168 \pm 0.894)^\circ/\mathrm{yr} \cdot x + (44.532 \pm 1.47)^\circ.$$

With $\chi^2/ndf = 13.58/5$ for the constant and $\chi^2/ndf = 11.78/4$ for the linear fit, both functions do not fit the data very well, still the quality of the constant fit is slightly higher.

Discussion

For the linear fit for both, the amplitudes as well as the phases, the slope is compatible with zero on the 1.4σ level. Considering this and the χ^2/ndf of both fits, the data do not support the hypothesis of time variation in the anisotropy pattern.

This corresponds to the result found within the 12-year analysis of combined data from AMANDA and IceCube [SGK+13].

Chapter 7

Discussion and outlook

7.1 Comparison with other experiments

Several astroparticle experiments have measured the sidereal anisotropy so far and published their results. Tab.7.1 shows a compilation of the amplitudes and phases from other experiments. Also listed are the median energy of the primary particles and the time period of the data collection.

Experiment	Energy	Amplitude ($\cdot 10^{-4}$)	Phase [°]	Year
EAS-TOP	100 TeV	2.6 ± 0.8	6 ± 18	1992-1999
SuperK	~ 10 TeV	6.64 ± 1.5	33.2 ± 13.3	1996-2001
Tibet AS-γ	> 3 TeV	3.2 ± 0.3	259.9 ± 46.5	2001-2005
Milagro	$4 - 7$ TeV	4.0 ± 0.07	104.3 ± 4.8	2000-2007
IceCube	14 TeV	6.4 ± 0.2	66.4 ± 2.6	2007-2008
AMANDA	~ 10 TeV	6.20 ± 0.16	44.2 ± 1.5	2000-2005

Table 7.1: Amplitudes and phases from other experiments also listed are the median energy of the primary particles and the time period of data collection ([A+07], [GHI+05], [AAB+06], [AAA+09], [Abb10])

The AMANDA-result shows a very good agreement in the amplitude with most experiments, being closest to the result of IceCube which is somehow expected because of the similar location of the the two experiments. However, the phases differ widely. Currently, there is no explanation for this fact.

A closer look at the results of IceCube and AMANDA shows an excellent agreement.

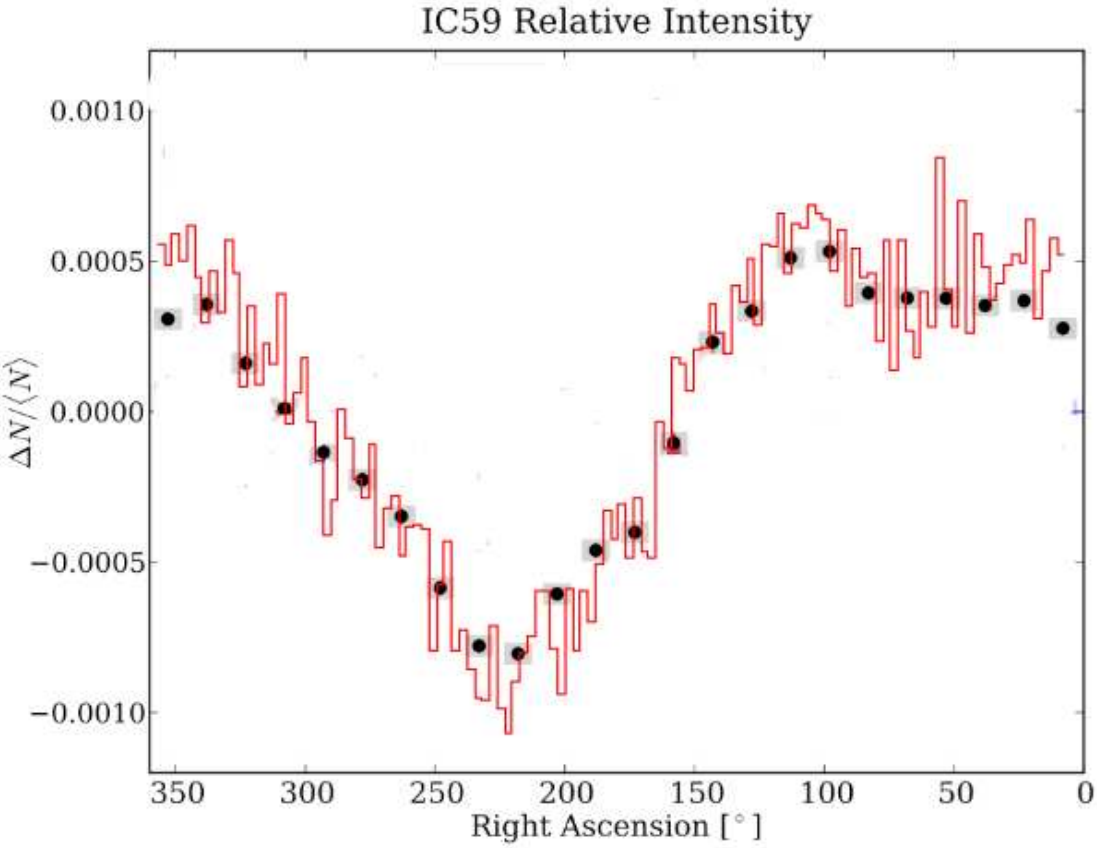

Figure 7.1: AMANDA (red line) and IceCube (black dots) result (IC results from [Abb10])

Fig.7.1 shows the RA-distribution of AMANDA for 2000-2005 as red line as well as the 1-d projection of the IceCube sky map as black dots. The analyses of AMANDA and IceCube have been carried out independently from one another.

7.2 Past problems and future plans

Past problems

In the beginning of this work, it was planned to present an analysis of the full data period of AMANDA II, which would have been 2000-2006. Unfortunately, it turned out that the data from 2006 could not be cleaned in a trustable way without losing too much data to make the analysis possible.

This is due to that in this year, the construction and calibration of the new detector at South Pole, IceCube was in full progress. This shows up in the counting rates as artificially high peaks:

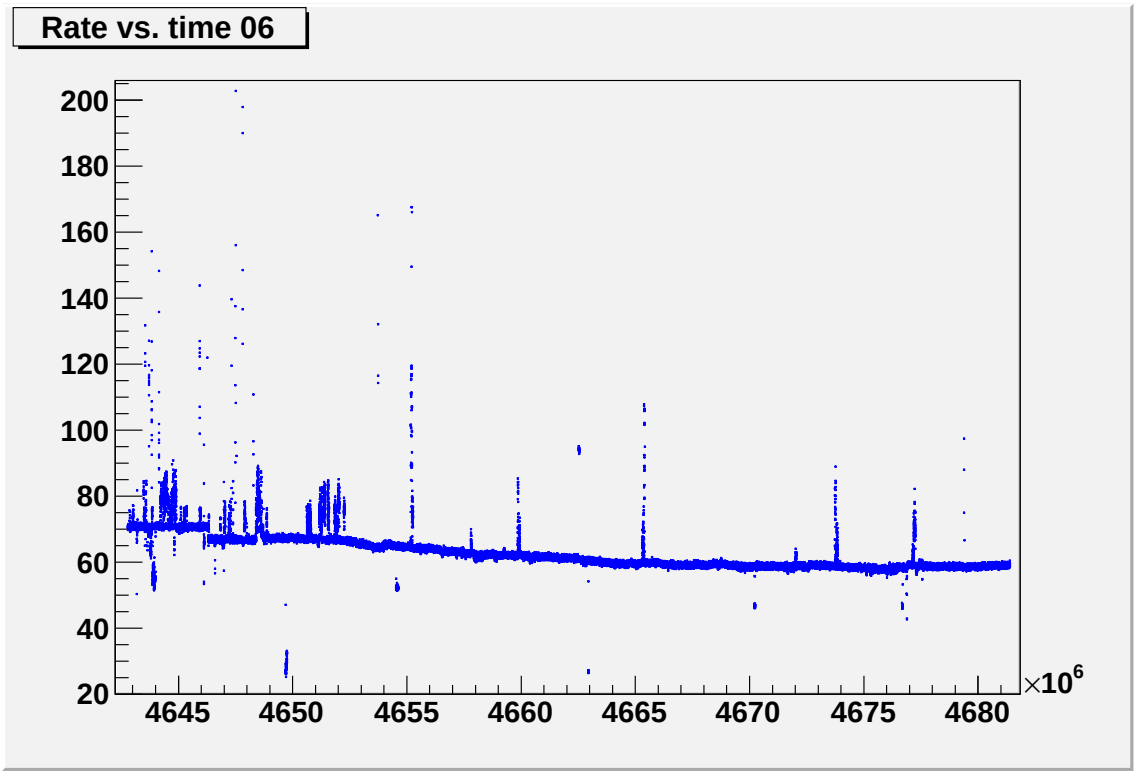

Figure 7.2: Counting rate 2006

Therefore the decision was taken to leave 2006 out of the analysis.

Future plans

Six years is only a very short time in cosmological scale. Still it is half of a solar cycle of data which could be analysed within this work. AMANDA is not taking data any longer since 2006, therefore, a further analysis of the time evolution of the anisotropy cannot be carried out. But AMANDA has its successor IceCube, which is taking data since 2007 at the almost same location with a much higher trigger rate and improved reconstruction techniques.

By today, AMANDA and IceCube have observed a complete solar cycle. First comparisons of the results from the two experiments show, that the analysis presented here can very well be continued with IceCube data, as independent analyses show a very good agreement regarding amplitude and phase of the observed anisotropy.

Fig. 7.3 shows the one-dimensional projections of relative intensity from the combined analysis of AMANDA and IceCube data for 2000 - 2012.

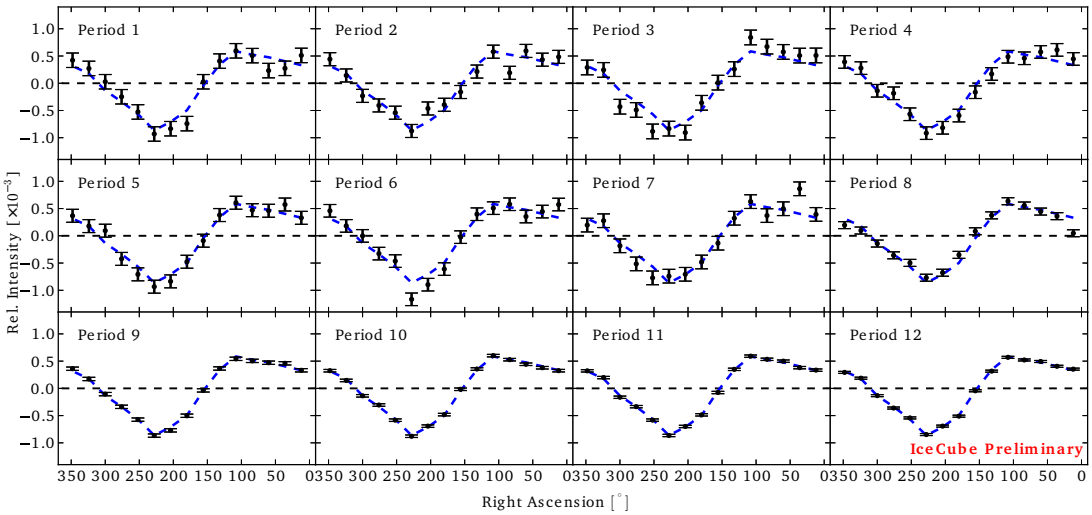

Figure 7.3: One-dimensional projections of relative intensity as a function of right ascension for 12 time periods covering the time between 02/13/2000 and 05/14/2012. As a reference, the average profile for the entire data set is shown as a dashed blue line. The uncertainties shown are only statistical. [SGK+13]

For the analysis of the time stability over the complete time interval, the profile of the anisotropy of each period was compared quantitatively to the global twelve-year average by means of a χ^2-test. No significant time variation in the observed anisotropy was found over the analysed 12 years.

7.3 Summary and conclusions

After careful data selection and stability studies have been carried out, 1- and 2-dimensional anisotropy analyses have been performed on the data collected by the AMANDA MuonDaq during the years 2000-2005. Each year was also studied separately.

It has been shown that AMANDA is able to see the galactic cosmic ray anisotropy as seen in other experiments before. The results in this work are in a good agreement with those of other experiments, especially an excellent agreement is reached with IceCube, a neutrino telescope located at the same site as AMANDA.

The cause of this anisotropy is not fully explained yet. Different theories have been put forward e.g. by [CG35], [EW06], [NFJ98] and others. A selection of anisotropy models has been presented in chapter 3. A full agreement with one of the described models is not observed. The low-energy models (3.1) are not expected to fit as these effects are only observable at energies outside the sensitivity of the AMANDA-detector. The same applies for the Cosmological Compton-Getting-Effect at the high end of the energy spectrum. The Compton-Getting model (3.2.2) does fit the order of magnitude

of the amplitude, but the data shows, that the anisotropy is not of a pure dipole structure as expected from Compton-Getting-Effect. Furthermore, the observed phase of the dipole anisotropy contradicts the predicted one. The NFJ-model (3.2.1) describes the anisotropy as a superposition of two kinds of anisotropy. This corresponds to the observation that the obtained results do not show a pure dipole structure. The picture of a galactic anisotropy and a superposed excess from other origin could explain the larger excess areas compared to deficit areas. Still the predicted positions of the maxima and minima fit only very roughly to the observation.

A significant temporal variation within the amplitudes or phases between 2000 and 2005 could not be observed. Also an extension of the period until 2012 using data from IceCube-Experiment do not show a significant change within the amplitudes and phases of the anisotropy [SGK+13].

The work has shown that AMANDA was not only a good neutrino telescope, but also a powerful instrument for cosmic ray research. The chosen analysis methods were closely related to the nature of the experiment, exploiting the unique location close to the geographical south pole.

Bibliography

[A+07] M. Aglietta et al. Eas-top: the cosmic ray anisotropy in the energy region $E_0 = 10^{14} - 10^{15}$ eV. In *Proc 30 th ICRC 111-111,2007*, 2007. 81

[AAA+04] J. Abraham, M. Aglietta, I. C. Aguirre, M. Albrow, D. Allard, I. Allekotte, P. Allison, J. Alvarez Muñiz, M. G. Do Amaral, M. Ambrosio, and et al. Properties and performance of the prototype instrument for the Pierre Auger Observatory. *Nuclear Instruments and Methods in Physics Research A*, 523:50–95, May 2004. 29

[AAA+09] A. A. Abdo, B. T. Allen, T. Aune, et al. The Large-Scale Cosmic-Ray Anisotropy as Observed with Milagro. *Astrophysical Journal*, 698:2121–2130, 2009, arXiv:astro-ph/0806.2293. 39, 43, 81

[AAA+10] J. Abraham, P. Abreu, M. Aglietta, C. Aguirre, et al. The fluorescence detector of the Pierre Auger Observatory. *Nuclear Instruments and Methods in Physics Research A*, 620:227–251, 2010. 30

[AAB+99] E. C. Andrés, P. Askebjer, S. W. Barwick, et al. The AMANDA neutrino telescope. *Nuclear Physics B Proceedings Supplements*, 77:474–485, May 1999, hep-ex/9809025. 48, 49

[AAB+00] E. Andres, P. Askebjer, S. W. Barwick, et al. The AMANDA neutrino telescope: principle of operation and first results. *Astroparticle Physics*, 13:1–20, March 2000, arXiv:astro-ph/9906203. 45, 47

[AAB+01] E. Andrés, P. Askebjer, X. Bai, et al. Observation of high-energy neutrinos using Čerenkov detectors embedded deep in Antarctic ice. *Nature*, 410:441–443, March 2001. 51

[AAB+04] T. Antoni, W. D. Apel, A. F. Badea, et al. Large-scale cosmic-ray anisotropy with KASCADE. *The Astrophysical Journal*, 604:687–692, 2004. 39, 40

[AAB+06] M. Amenomori, S. Ayabe, X. J. Bi, et al. Anisotropy and Corotation of Galactic Cosmic Rays. *Science*, 314:439–443, 2006, arXiv:astro-ph/0610671. 40, 42, 43, 81

[Abb10] Abbasi, R. U. and the IceCube-Collaboration. Measurement of the Anisotropy of Cosmic Ray Arrival Directions with IceCube. *The Astrophysical Journal*, 718:L194–L198, 2010, arXiv:astro-ph/1005.2960. 43, 74, 81, 82

[Abb12] Abbasi, R. U. and the IceCube-Collaboration. Observation of anisotropy in the galactic cosmic-ray arrival directions at 400 TeV with icecube. *The Astrophysical Journal*, 746:33, 2012, arXiv:astro-ph/1109.1017. 42

[ALS77] W. I. Axford, E. Leer, and G. Skadron. The acceleration of cosmic rays by shock waves. In *International Cosmic Ray Conference*, volume 11 of *International Cosmic Ray Conference*, pages 132–137, 1977. 10

[Amb03] G. Ambrosi. AMS, a particle detector in space: results from the precursor flight and status of AMS-02. *Nuclear Physics B Proceedings Supplements*, 125:236–244, September 2003. 29

[BAD+11] R. Boninho, V. V. Alekseenko, O. Deligny, et al. The East-West Method to Search for Large-scale Anisotropies of Cosmic Rays. *The Astrophysical Journal*, 738:67, 2011, arXiv:astro-ph/1106.2651. 37

[Bel78a] A. R. Bell. The acceleration of cosmic rays in shock fronts. I. *Monthly Notices of the Royal Astronomical Society*, 182:147–156, January 1978. 10

[Bel78b] A. R. Bell. The acceleration of cosmic rays in shock fronts. II. *Monthly Notices of the Royal Astronomical Society*, 182:443–455, February 1978. 10

[BGG05] V. Berezinsky, A. Z. Gazizov, and S. I. Grigorieva. Dip in UHECR spectrum as signature of proton interaction with CMB [rapid communication]. *Physics Letters B*, 612:147–153, April 2005, arXiv:astro-ph/0502550. 35

[Ces80] C. J. Cesarsky. Cosmic-ray confinement in the galaxy. *Annual review of astronomy and astrophysics*, 18:289–319, 1980. 16

[CG35] A. H. Compton and I. A. Getting. An Apparent Effect of Galactic Rotation on the Intensity of Cosmic Rays. *The Physical Review*, 47:817–821, 1935. 33, 34, 35, 84

[Chi03] D. A. Chirkin. *Cosmic Ray Energy Spectrum Measurement with the Antarctic Muon and Neutrino Detector Array (AMANDA)*. PhD thesis, UNIVERSITY of CALIFORNIA at BERKELEY, 2003. 59

[col03] Tibet collaboration. Tibet as-gamma experiment. `http://www.icrr.u-tokyo.ac.jp/em/`, 2003. 30

[col05] HESS collaboration. H.e.s.s.-teleskop entdeckt kosmische uhr. `http://www.mpi-hd.mpg.de/hfm/HESS/pages/press/old/PressRelease/LS5039Press-2006/PressRelease_D.html`, 2005. 30

[CW73] R. Cowsik and L. W. Wilson. Is the Residence Time of Cosmic Rays in the Galaxy Energy-Dependent? In *International Cosmic Ray Conference*, volume 1 of *International Cosmic Ray Conference*, page 500, 1973. 17

[DM38] A. De Moivre. *The Doctrine of Chances*. Woodfall, 2 edition, 1738. 37

[EW06] A. D. Erlykin and A. W. Wolfendale. The anisotropy of galactic cosmic rays as a product of stochastic supernova explosions. *Astroparticle Physics*, 25:183–194, 2006. 36, 84

[Fer49] E. Fermi. On the Origin of the Cosmic Radiation. *The Physical Review*, 75:1169–1174, 1949. 10

[Flü01] E. O. Flückiger. Lecture notes, 2001. 32

[GA68] L. J. Gleeson and W. I. Axford. The compton-getting effect. *Astrophysics and Space Science*, 2:431–437, 1968. 35

[Gai90] T. K. Gaisser. *Cosmic rays and particle physics*. Cambridge University of Arizona Press, Cambridge, GB, 1 edition, 1990. 13, 14, 18, 20

[GHB+05] K. M. Górski, E. Hivon, A. J. Banday, B. D. Wandelt, F. K. Hansen, M. Reinecke, and M. Bartelmann. HEALPix: A Framework for High-Resolution Discretization and Fast Analysis of Data Distributed on the Sphere. *The Astrophysical Journal*, 622:759–771, 2005, arXiv:astro-ph/0409513. 73, 93

[GHI+05] G. Guillian, J. Hosaka, K. Ishihara, et al. Observation of the anisotropy of 10 tev primary cosmic ray nuclei flux with the super-kamiokande-i detector. 2005, arXiv:astro-ph/0508468v1. 33, 40, 41, 43, 81

[Hel08] K. Helbing. Lecture notes, 2008. 9, 10

[HL88] G. Halzen and J. G. Learned. High Energy Neutrino Detection in Deep Polar Ice. In *Proceedings of the 5th International Symposium on Very High Energy Cosmic Ray Interactions, Poland, 1988*, 1988. 47

[Hun99] S. Hundertmark. Up- and down-going muons in the AMANDA-B4 prototype detector. *International Cosmic Ray Conference*, 2:12, 1999. 49

[I+05] M. Israel et al. Nasa stratospheric balloons. `http://sites.wff.nasa.gov/code820/balloonroadmapreport.pdf`, 2005. 29

[Kry77] G. F. Krymskii. A regular mechanism for the acceleration of charged particles on the front of a shock wave. *Akademiia Nauk SSSR Doklady*, 234:1306–1308, June 1977. 10

[KS06] M. Kachelrieß and P. D. Serpico. The Compton-Getting effect on ultra-high energy cosmic rays of cosmological origin. *Physics Letters B*, 640:225–229, 2006, arXiv:astro-ph/0605462. 35

[Lin75] J. Linsley. Fluctuation effects on directional data. *Physical Review Letters*, 34:1530–1533, 1975. 37

[LM00] J. G. Learned and K. Mannheim. High-Energy Neutrino Astrophysics. *Annual Review of Nuclear and Particle Science*, 50:679–749, 2000. 25

[Lon81a] M. S. Longair. *High Energy Astrophysics*, volume 2. The University of Arizona Press, Tucson, USA, 2 edition, 1981. 10, 12, 15

[Lon81b] M. S. Longair. *High Energy Astrophysics*, volume 1. The University of Arizona Press, Tucson, USA, 2 edition, 1981. 21, 22, 23, 24, 25, 27

[Lor99] E. Lorenz. Air shower Cherenkov detectors. *Nuclear Instruments and Methods in Physics Research A*, 433:24–33, August 1999. 30

[MBP+94] P. Mock, S. Barwick, R. Porrata, et al. AMANDA Results from the 1993-94 South Pole Deployment. In *American Astronomical Society Meeting Abstracts #184*, volume 26 of *Bulletin of the American Astronomical Society*, page 888, May 1994. 49

[Mol09] S. Mollerach. Techniques to study cosmic rays anisotropies. 2009, arXiv:astro-ph/0902.3601v1. 31, 32, 35, 37

[NFJ98] K. Nagashima, K. Fujimoto, and R. M. Jacklyn. Galactic and heliotail-in anisotropies of cosmic rays as the origin of siedereal daily variation in the energy region $< 10^4$ GeV. *Journal of Geophysical research*, 103:17429–17440, 1998. 32, 33, 84

[Noz04] M. Nozaki. BESS-Polar. *Nuclear Instruments and Methods in Physics Research B*, 214:110–115, January 2004. 29

[Pie08] Pierre Auger Collaboration. Observation of the suppression of the flux of cosmic rays above $4 \cdot 10^{19}$eV. *Physical Review Letters*, 101(6):061101, 2008. 20

[Pie12] Pierre Auger Collaboration. Large scale distribution of arrival directions of cosmic rays detected above 10^{18} eV at the pierre auger observatory. 2012, arXiv:astro-ph/1210.3736v2. 36

[PJSS05] V. S. Ptuskin, F. C. Jones, E. S. Seo, and Sina R. Cosmic Rays in Galactic Diffusion Model with random Supernova Outbursts: Statistical Fluctuations, Anisotropy, Very High Energy Electrons. In *International Cosmic Ray Conference*, volume 3 of *International Cosmic Ray Conference*, page 193, 2005. 31

[Pot13] M. Potgieter. Solar Modulation of Cosmic Rays. *Living Reviews in Solar Physics*, 10:3, June 2013, 1306.4421. 31

[PSP10] P. Picozza, R. Sparvoli, and PAMELA Collaboration. The instrument PAMELA for antimatter and dark matter search in space. *Nuclear Instruments and Methods in Physics Research A*, 623:672–676, November 2010. 29

[RP75] I. L. Rasmussen and B. Peters. The nuclear composition of cosmic rays at their source in a closed galaxy. *Nature*, 258:412, December 1975. 17

[Sem06] B. Semburg. personnel communication, 2006. 50

[SGK+13] M. Santander, M. Gurtner, T. Karg, et al. Study of the time-dependence of the cosmic-ray anisotropy with AMANDA and IceCube. In *Proc 33 rd ICRC,2013*, 2013. 80, 84, 85

[Sim83] J. A. Simpson. Elemental and Isotopic Composition of the Galactic Cosmic Rays. *Annual Reviews of Nuclear Particle Science*, 33:323–382, 1983. 18

[Sim00] J. A. Simpson. The Cosmic Ray Nucleonic Component: The Invention and Scientific Uses of the Neutron Monitor - (Keynote Lecture). *Space Science Reviews*, 93:11–32, July 2000. 28

[Ste01] P. Steffen. Direct-walk a fast track search algorithm without hit cleaning. Amanda internal report, 2001. 58, 59

[Swo97] S. Swordy. Astroparticle physiscs at chicago. `http://astroparticle.uchicago.edu/`, 1997. 19

[Tep09] A. Tepe. *Hardware integration of the AMANDA into the IceCube Neutrino Telescope and search for supersymmetric particles with the IceCube Neutrino Telescope*. PhD thesis, Bergische Universität Wuppertal, 2009. 55

[Wag04] W. Wagner. *Design and Realisation of a new AMANDA Data Acquisition system with Transient Waveform Recorders*. PhD thesis, Universiät Dortmund, 2004. 46, 54

Acknowledgments

First and foremost I have to thank to Prof. Dr. Ch. Wiebusch for inviting me to Wuppertal and inspiring me to work on this fascinating topic, and to Prof. Dr. K. H. Kampert for overtaking the supervision and support during all the years. My severe thanks goes as well to all my colleagues I have met during the years, it was always a pleasant working atmosphere within the group. I would like to mention especially Simon Robbins, Andreas Tepe, and Timo Karg for their scientific and technical support.

I should not forget my colleagues from the time after university and to my family and friends who always encouraged me to finish this thesis.

Last but not least, I am also very grateful to my beloved partner for his love and support throughout the years. Without you this would not have been possible.

Some of the results in this work have been derived using the HEALPix [GHB+05] package.

Selbständigkeitserklärung

Hiermit versichere ich, daß ich diese Arbeit nur unter Zuhilfenahme der angegebenen Quellen und Hilfsmittel selbständig angefertigt habe.

Ort, Datum

Maria Gurtner